LC3B is lipidated to large lipid droplets for autophagic degradation

Mohyeddine Omrane[1,#], Kalthoum Ben M'Barek[1,#], Alexandre Santinho[1], Nathan Nguyen[2], Shanta Nag[2], Thomas Melia[2], Abdou Rachid Thiam[1,*]

[1] Laboratoire de Physique de l'École Normale Supérieure, ENS, Université PSL, CNRS, Sorbonne Université, Université de Paris, F-75005 Paris, France

[2] Department of Cell Biology, Yale University School of Medicine, New Haven, CT

# these authors contributed equally to this work

*Correspondence to:

Abdou Rachid Thiam

Laboratoire de Physique Statistique,

Ecole Normale Supérieure,

PSL Research University,

75005 Paris Cedex 05, France

thiam@ens.fr

Abstract.

Lipid droplets (LDs) store lipids and proteins degraded during scarcities through autophagy and lysosomal pathways. How mechanistically such degradation happens remains unclear. Here, we report that long-term starvation triggers the binding of the E2 enzyme Atg3 to the surface of specific and ultra-large LDs in 3T3 adipocyte cells. Atg3 specifically lipidated LC3B to these LDs. In the ATG5-deficient DU145 prostate cancer cells, lacking autophagy, LDs' production also led to LC3B lipidation to LDs, which, remarkably, restored an autophagic flux. Agreeing with these findings, ATG3 bound to the surface of purified and reconstituted LDs and, with Atg7, mediated LC3B lipidation. Finally, we found that the LD-lipidated LC3B recruits collections of acidified LC3B-membranes, indicating the ongoing degradation of proteins and lipids on the LDs. Collectively, our data reveal a noncanonical autophagy mechanism, resembling LC3-associated phagocytosis, wherein LC3B is lipidated to the phospholipid monolayer of oil/water interfaces and serves as a receptor for the degradation of sizeable LDs.

Introduction

Autophagy is a catabolic process degrading cellular components and triggered by several cues such as energy deprivation or cellular stresses (Mizushima and Komatsu, 2011). A major autophagic pathway is macroautophagy, wherein an autophagosome, a double-vesicle membrane phagophore, isolates compounds from the cytosol and delivers them to lysosomes for degradation (Feng et al., 2014; Mizushima et al., 2002). The formation of the autophagosome proceeds in multiple steps (Feng et al., 2014; Mizushima, 2020; Sawa-Makarska et al., 2020): initiation and nucleation of a pre-autophagosomal structure (PAS)(~ 100 nm)(Lamb et al., 2013), elongation of the membrane and encapsulation of cargos, closure of the double-vesicle (~ 0.5 - 1.5 μm in size), i.e., the completed autophagosome (Klionsky and Eskelinen, 2014; Yim and Mizushima, 2020). These steps involve many autophagy (Atg) related enzymes and take place at specific endoplasmic reticulum (ER) subregions (Melia et al., 2020; Nakatogawa, 2020).

The PAS maturation and recognition of cargos require the lipidation of a ubiquitin-like protein Atg8 to phosphatidylethanolamine (PE) onto the double-membrane (Mizushima et al., 2011; Nath et al., 2014). In mammals, there are two ATG8 subfamilies, the microtubule-associated protein 1 light chain 3 A (also known as MAP1LC3)(LC3A), LC3B (the most ubiquitous), LC3B2 and LC3C, and the GABA type A receptor-associated protein (GABARAP) and GABARAP-like proteins, GABARAPL1 and GABARAPL2 (Shpilka et al., 2011). The lipidation reaction involves the ATG16L1/ATG5-ATG12 complex (Dooley et al., 2014; Gammoh et al., 2013; Nishimura et al., 2013). ATG16 binds to the PAS through interactions with FIP200, WIPI2, and PI3P on the membrane. Bound ATG16 recruits ATG5-ATG12, which then recruits Atg3 onto the membrane, the E2 enzyme catalyzing Atg8 lipidation (Ichimura et al., 2000). Finally, Atg7, an E1 protein (Kim et al., 1999), activates and delivers Atg8 to Atg3, which lipidates it to PE onto the phagophore (Martens and Fracchiolla, 2020).

Beyond autophagosomes, LC3 can also conjugate to PE on single bilayer membranes in noncanonical autophagy routes such as LC3-associated phagocytosis (Heckmann and Green, 2019). This pathway mediates the cellular degradation of large components internalized by phagocytosis (Martinez et al., 2011), and the lipidated LC3 is thought to play a role in recruiting lysosomes (Herb et al., 2020). This noncanonical autophagic pathway does not produce autophagosomes and does not implicate critical autophagic enzymes such as Atg9 or the ULK complex (Herb et al., 2020) but requires all of the upstream lipidation machinery, including ATG16L1/ATG5-ATG12. The existence of this pathway indicates that autophagic proteins might function in other processes than autophagosome biology (Galluzzi and Green, 2019). Intriguingly, several autophagy proteins have been localized to the surface and around lipid

droplets (LDs): Atg2, DFCP1, Atg14L, and possibly LC3 (Gao et al., 2019; Li et al., 2019; Pfisterer et al., 2014; Shibata et al., 2009, 2010; Velikkakath et al., 2012). Such LD localizations support the model of functional crosstalk that is as yet not understood between macroautophagy, hereafter termed autophagy, and LDs.

LDs are structurally unique cellular organelles because of their neutral lipid oil core, containing triglycerides mainly and surrounded by a phospholipid monolayer (Thiam et al., 2013). LDs function primarily in maintaining cellular energy balances but have several non-metabolic functions, e.g., protein quality control, gene expression, development, etc. (Welte and Gould, 2017). LD functions are strongly attuned to proteins bound to their surface (Dhiman et al., 2020). Two major classes of proteins target LDs: a soluble class of proteins, which often bear amphipathic helix (AH) motifs or lipid anchors, and monotopic membrane proteins, which often move from the ER to LDs via physical contiguities (Caillon et al., 2020; Kory et al., 2016; Olzmann and Carvalho, 2018; Thiam and Dugail, 2019). Most autophagic proteins reported to target LDs come from the cytosol, except DFCP1, from the ER (Li et al., 2019).

Autophagic proteins may regulate LD biogenesis (Shibata et al., 2009) and catabolism (Singh and Cuervo, 2012). Conversely, LDs may regulate autophagy by fueling lipids for autophagosome biogenesis (Dupont et al., 2014; Li et al., 2015; Schütter et al., 2020; Shpilka et al., 2015; Velázquez et al., 2016). Furthermore, the adipose triglyceride lipase (ATGL), which acts on the LD surface, has an LC3 interacting motif (LIR), and its activity modulates Sirtuin 1, an autophagy regulator (Martinez-Lopez et al., 2016; Sathyanarayan et al., 2017). During energy scarcities, LDs can undergo lipophagy (Singh et al., 2009), a process by which an LD is engulfed by an autophagosome that subsequently fuses with lysosomes. How LD-autophagosome interaction is mediated in lipophagy is unknown (Gatica et al., 2018). During energy depletion in the liver, ATGL hydrolyses triglycerides to reduce LDs' size to a point they can fit in autophagosomes (Schott et al., 2019). Smaller LDs, below 1µm, are majorly found in autophagosomes and autolysosomes (Schott et al., 2019) and are so far the ones known to be targeted by lipophagy. Altogether, these observations indicate that depending on metabolic cues, autophagy and LDs talk to each other through diverse channels, which are yet not well established.

In this study, we focus on the connection between LDs and autophagosomes during energy deprivation. In several mammalian cells, particularly in 3T3 adipocytes, we found LC3B localized to few and large LDs, up to 25 µm in size. In vitro reconstitutions and cell experiments showed that LC3B is lipidated to LDs' surface by the minimal Atg3,7 machinery. Our findings indicate the existence of a noncanonical autophagy pathway using the LD surface as a lipidation station, essential for autophagy and LD degradation.

Results.

LC3B localizes to large LDs during long-term nutrient deprivation

Adipocytes are the primary lipid storage cells and contain large LDs. We studied the interaction of autophagosomes and LDs in this cell line upon nutrient deprivation. LC3B is the most abundant Atg8 protein in mammals and is an autophagosome marker, yet not exclusively (Klionsky et al., 2021). Differentiated 3T3 adipocytes were infected by an eGFP-LC3B adenovirus and grown in Earle's balanced salts (EBSS), nutrient-deprived media, free of bovine serum albumin (BSA), for 72hs.

During nutrient starvation, we found that small LDs, ~µm in size, had a faint LC3B signal and were positive for lysotracker (Figure S1A). These LDs were likely undergoing lipophagy, i.e., LD degradation in autolysosomes (Figure S1A). However, we observed a striking phenotype wherein LC3B was detected around ultra-large LDs, tens of µm in size (Figure 1A and Figure S1B), at 24, 48, and 72hs (Figure 1A-D). This localization persisted when BSA was added to the culture medium to capture released fatty acids by starvation (Figure S1C), excluding that LC3B localization to the large LDs was linked to de novo re-esterification of the liberated fatty acids. When the cells were grown in DMEM or starved for two hours only, the eGFP-LC3B signal on the ultra-large LDs was not noticed. In many cases, the LC3B signal on LDs overlapped with Plin1, a standard adipocyte LD surface marker (Figure S1D). However, the eGFP-LC3B signal on the LDs was often inhomogeneous, with both a uniform LC3B signal on the LD surface (Figure 1A) and another more intense accumulation of LC3 signal immediately adjacent or adhering to the LDs (Figure S1B).

The LC3B-positive LD phenotype increased during nutrient starvation, with up to 20% of the cells at 48hs and 72hs (Figure 1C). Likewise, the percentage of the large LDs displaying an LC3B ring increased along with nutrient starvation, up to 6% at 48 and 72hs (Figure 1D). Relatively to the LDs' size distribution, LC3B more specifically targeted the large LDs' subset (Figure 1E and F). As these observations were made with overexpressed eGFP-LC3B, we looked at endogenous LC3B at 48h and found it around larger LDs, again only in EBSS and not in complete media (Figure 1G). On purified LDs in the EBSS condition, we found the presence of lipidated LC3B-II, along with a smaller amount of LC3B-I (Figure 1H).

In diverse cell lines, lipophagy happens with small LDs in the range of 1 µm or less (Li et al., 2016; Schott et al., 2019; Singh et al., 2009). Here, the LDs positive for LC3B were up to ~25µm in size. We measured the size distribution of the LD-negative vs. LD-positive LC3B signals (Figure 1I). We found a narrow 1.5 µm-centered distribution for LD-negative LC3 puncta, which are likely autophagosomes or autolysosomes, whose size is consistent with our

measured dimensions (Figure 1I) (Jin and Klionsky, 2014; Klionsky et al., 2021). The size distribution of the LD-positive LC3 signal showed a greater spread from 2-25μm (Figure 1D and 1J). Altogether, these data support that the LC3B signal on the large LDs might be distinct from LC3B on autophagosomes.

Like LC3B, GABARAPL proteins undergo post-translational lipid modification onto phagophore membranes (Thukral et al., 2015). In the 3T3 cells maintained in EBSS for 48h, we immuno-stained the endogenous GABARAPs with an antibody capable of recognizing them. No GABARAP ring around large LDs was detected. We repeated the experiments by treating the cells with chloroquine or rapamycin to induce more autophagosomes, but the GABARAP signal was still absent from the large LDs (Figure S1E).

Finally, we wanted to know whether other cell lines display a preferential localization of LC3B to the largest LD. We worked with liver hepatoma 7 (Huh7) and HeLa cells which were fed with oleic acid (OA) for 24h before they were maintained in EBSS for 48h (Figure 1K, 1L). Although these cells could not make LDs as big as the larger adipocyte LDs, most of the LDs that displayed a clear LC3B ring were amongst the largest ones, 2μm and over in size (Figure 1K). As in adipocytes, the frequency of this phenotype increased upon nutrient starvation (Figure S1F-H).

Altogether, our results point to a model that specific large LDs in cells incubated in EBSS for an extended period recruit LC3B to their surface.

LC3B LD association is independent of known-LC3B interactors and autophagosomes

We wanted to know whether the LC3B signal on the large LDs arose from LC3B interaction with proteins on LDs or the close apposition of autophagosomes.

Proteins with LIR motifs could recruit LC3 to the LD surface. ATGL, whose activity regulates lipophagy in mice liver, has an LIR motif (Martinez-Lopez et al., 2016), and we hypothesized that it could recruit LC3B. Overexpression of ATGL in Huh7 did not alter the LC3B LD-localization phenotype under our nutrient starvation conditions (Figure S2A-D). We next studied the impact of Plin1, the major adipocyte LD protein, marking large LDs (Wolins et al., 2006). Plin1 has LIR sequences on its C-terminal region, i.e., YVPL and YSQL, and could, therefore, interact with LC3B. To test this, we expressed mCherry-Plin1 in Huh7 cells, which do not express Plin1. During EBSS starvation, Plin1 localized to all LDs, but the LC3 LD localization was not increased, indicating that Plin1 did not mediate LC3 recruitment to LDs (Figure S2E-G). Next, we studied one of the major LC3 interactors, P62, sequestosome-1, encoded in humans by the SQSTM1. P62 is the adaptor protein bound to most ubiquitinated

proteins or organelles targeted for degradation (Pankiv et al., 2007). The LC3 ring signals around the large LDs could be due to LC3 interaction with P62 bound to ubiquitinated LD proteins. To investigate this model, we virally co-transfected the differentiated 3T3 adipocytes with eGFP-LC3 and mRFP-P62 and incubated the cells in EBSS for 48h. We found clear LC3 signals around LDs, but most were devoid of P62 (73% of cases; Figure 2A and S2H), especially larger ones. In the remaining 17%, we observed LC3 colocalizing with P62 more frequently on smaller LDs, although not completely (Figure 2A, B). We also find LC3B and P62 colocalized near LDs but distinct from the LC3B signal lacking P62 found on LDs (Figure 2C, 2D). This observation suggests that different pools of LC3B were on LDs and autophagosome structures. Lastly, the overexpression of mRFP-P62 did not increase the percentage of LDs or cells with LC3- positive LDs (Figure S2H-J). The P62/LC3 colocalization Pearson's index sharply decreased on LDs compared with cytosolic puncta (Figure S2K). Altogether, these observations support that LC3 is not recruited to the large LDs by these proteins.

Next, we modulated autophagy pathways to study whether they alter LC3 localization to the large LDs of 3T3 adipocytes. We first targeted Atg5 by a lentivirus shRNA to block autophagosome formation. We then subjected the cells to nutrient starvation in EBSS for 48h. The percentage of cells with LC3B-positive large LDs decreased compared with non-targeting shRNA transfected cells. Yet, the fraction of large LC3B-positive LDs per cell in this condition remained constant (Figure 2 E-I). The decreased percentage of cells with the LC3B-localized LDs' phenotype suggests that the LC3B LD signal may somewhat depend on autophagosomes' capacity to form. To challenge this hypothesis, we decided to interfere with upstream and downstream factors regulating autophagosomes. First, we treated the cells with rapamycin for 48h to inhibit mTOR, thereby boosting autophagy; no enhancement in the number of large LC3B-positive LDs ensued (Figure S2L). Second, we treated the cells with bafilomycin to block the fusion of autophagosomes with lysosomes. Many autophagosomes accumulated, but the fraction of large LC3B-positive LDs per cell was likewise unaltered (Figure 2J). Lastly, we treated the cells with Spautin-1, which degrades the Vps34 PI3 kinase complex, essential to triggering autophagosome formation (Klionsky et al., 2021; Liu et al., 2011). Likewise, we did not see any alteration in the phenotype: LC3B still displayed a clear LD protein-like signal, and the number of large LDs positive for LC3B was intact (Figure 2K-M); western blot analysis confirmed a decrease in LC3B lipidation due to Spautin-1 while LC3B-II was still present in the LD fraction (Figure 2N). Finally, LC3B was found around large LDs when mouse adipocytes were treated with 3-MA and starved (Le Lay et al., 2010); when we treated cells with 3-MA, we still found cells with LC3B localized to larger LDs (Figure 2SM). Altogether, these findings indicate that the LC3 on LDs is independent of the autophagosome formation and might depend on Atg5 in this cell line. Atg5 shRNA in these differentiated 3T3

adipocyte cells may alter other factors beyond autophagosome formation in an inhibitory way to LC3B LD localization.

ATG3 is recruited to lipid droplet surface during nutrient starvation

Our above data suggest that the LC3B signal on LDs is distinct from LC3B on autophagosomes and not due to interactions with the above-tested proteins. Also, in the LD fraction of 3T3 adipocytes cells, we found LC3B-II (Figure 1H). Thus, we hypothesized that LC3B is lipidated to the surface of the LDs. An immediate consequence of this hypothesis is that Atg3, which catalyzes LC3 lipidation to PE, should be on the surface of LDs.

Western blot analysis of LDs recovered at 48h nutrient starvation showed a clear Atg3 signal, in contrast to the non-starved situation (Figure S3A); also, LC3B-II was present on the LD fraction (Figure S3A). Then, we immunostained at 48h endogenous Atg3 and LC3B in differentiated 3T3 adipocytes under “feeding” (DMEM) or nutrient starvation (EBSS). We found endogenous Atg3 recruitment around LDs, together with endogenous LC3B (Figure 3A, S3B). When we treated the cell with 3-MA in the starvation condition to block autophagosome formation, endogenous ATG3 still localized around LDs (Figure 3B, S3C), supporting that Atg3 was directly recruited to the LDs’ surface.

To further confirm Atg3 binding to LDs, we worked with Huh7 and HeLa cells fed with OA and maintained in EBSS for 48h. We found that endogenous Atg3 localized to the surface of larger LDs also (Figure 3D), together with eGFP-LC3B. We then overexpressed either eGFP-ATG3 or ATG3-DsRed in Huh7 cells. In both cases, we found clear recruitment of ATG3 to few and larger LDs only (Figure 3E, F), as for LC3-II, and no recruitment happened in the fed state (Figure S3D). Then, we co-transfected Atg3-DsRed and LC3-eGFP to study their colocalization. In 48h in EBSS, we found instances where few large LDs recruited Atg3, but no LC3B signal was detected. This observation is a piece of solid evidence that the Atg3 signal on LDs did not come from autophagosomes but, instead, its direct binding to LDs (Figure 3G). In this experiment, either LC3 was not yet lipidated, or Atg3-DsRed had reduced catalytic activity since the lipidation reaction is mediated by the Atg3 C-terminal domain (Ichimura et al., 2000), here tagged with DsRed.

If Atg3 lipidates LC3B-II to LDs, its inactivation would decrease LC3B LD localization. We transfected differentiated adipocytes with a specific ATG3 shRNA and non-targeting shRNA and then subjected them to EBSS nutrient starvation for 48h. LC3 LD localization was almost abolished in the ATG3 shRNA transfected 3T3 cells (Figure 3H-L). The same observation was

made in Huh7 (Figure S3E-H)). This data supports that proteins did not directly recruit LC3B on the LD surface, and Atg3 presence is required for LC3B LD surface localization.

Atg3 binds to model LDs enriched in PE

The LD surface is permissive to the binding of amphipathic helix (AH) motifs, in part, because of the oil/water interface of high surface tension (Thiam and Dugail, 2019). Indeed, such tension is decreased by the non-specific adsorption of amphiphilic molecules (Thiam and Dugail, 2019). Atg3 has an N-terminus AH acting as a membrane curvature sensor (Nath et al., 2014; Nguyen et al., 2017) and, therefore, possibly a phospholipid packing sensor too. Interestingly, the size of LDs depends on the phospholipid composition (Ben M'barek et al., 2017). In particular, PE, which is required for LC3B lipidation, promotes the formation of large LDs (Ben M'barek et al., 2017). Therefore, we sought to test if Atg3 can associate with LDs' oil/water surface and how PC and PE, major LD phospholipids, modulate such binding.

We opted for in vitro reconstitution. In a buffer solution, we generated droplets made of triolein (Figure 4A), the major neutral lipid, and added purified Atg3-YFP. We observed that Atg3 is bound to the surface of the droplets (Figure 4B), suggesting that it can by itself associate with LDs. Next, we made the model LDs decorated by PC/PE at different ratios, 10/0, 7/3, 5/5, and 3/7. For each condition, we prepared different triolein-in-buffer droplets with a PC/PE coverage ranging from 0.005% to 0.2% (w/w to triolein), mixed with 1% Rhodamine-PE (Rh-PE) to report for the phospholipid density (Chorlay and Thiam, 2020): the higher the rhodamine signal, the higher the phospholipid density (Figure 4C). We then added Atg3-YFP to the droplets and observed its binding to the artificial LDs. The level of binding depended on the phospholipid density (Figure 4C), suggesting that the protein preferentially associates with monolayers depleted with phospholipid. For each PC/PE condition, we reported the relative amount of bound Atg3 as a function of the phospholipid coverage (Figure 4D and Figure 4SA). From this representation, we estimated the concentration of phospholipids at which half of the maximum binding was reached, i.e., concentration $C_{½}$ (Figure 4D, S4A). We found that increasing PE levels led to higher Atg3 binding to the droplets (Figure 4E), indicating that Atg3 associates more effectively with droplets rich in PE. Floatation assays carried with sonicated liposomes or droplets with various PC/PE ratios showed similar results confirming that PE promotes Atg3 binding to both bilayers and droplet monolayers (Figure 4F).

Next, we used a tensiometer approach, enabling us to characterize the adsorption of proteins to oil/water surfaces (Figure S4B) (Ajjaji et al., 2019; Small et al., 2009) and study the binding of non-tagged Atg3. To do so, we generated a triolein/buffer surface and added purified Atg3. The protein was recruited to the triolein/buffer interface since surface tension dropped down,

from ~32mN/m, i.e., triolein/buffer-free interface, to an equilibrium value of ~18mN/m, i.e., protein-adsorbed interface (Figure S4C). We then compressed this protein-adsorbed interface rapidly to lateral condense the protein layer. Consequently, surface tension rapidly decreased because the protein was lateral condensed, thereby better masking the interface (Figure S4D). However, this was not an equilibrium state: over time, surface tension re-increased to a new equilibrium, as Atg3 was falling off from the interface so that the protein monolayer relaxed (Ajjaji et al., 2019; Small et al., 2009) (Figure S4E-F). We repeated the above experiment with PC/PE (1/1), initially decorating the interface (Figure S4G). The compression step led to a less remarkable Atg3 fall-off, suggesting that PC/PE might promote Atg3 retention to the droplet surface (Figure S4G-H).

Altogether, our above data indicate that Atg3 can bind itself to LD's surface, likely via its N-terminal AH (Nath et al., 2014). PE, required for LC3 lipidation and promoting large LDs, favored more Atg3 binding to the model LD surfaces.

The Atg16,5-12 complex mediates Atg3 bilayer recruitment (Mizushima, 2020), while it was not required for the Atg3 LD association. Therefore, we sought to compare Atg3 binding efficiency between a bilayer and a droplet monolayer within the same system. For this purpose, we used the droplet embedded vesicle (DEV) system consisting of the incorporation of a neutral lipid droplet into a giant bilayer vesicle (GUV) (Chorlay et al., 2020), here made of 7/3 PC/PE. We then added Atg3-YFP to the buffer solution of the DEV and found that Atg3 was recruited exclusively to the model LD and not to the bilayer (Figure 4G). These data demonstrate that Atg3 cannot solely target a bilayer with a relevant PC/PE composition unless a high curvature is induced (Nath et al., 2014). Instead, for model LDs with the same phospholipid composition, Atg3 can bind by itself, regardless of curvature, partly because of the lower phospholipid density on the model LD (Figure 4H) (Caillon et al., 2020; Chorlay and Thiam, 2020).

Atg3 lipidates LC3 to LDs.

We asked whether Atg3 recruitment can drive LC3B lipidation to LDs. To test this, we first purified LDs from the 3T3 adipocytes and mixed them with a buffer solution containing Atg3, Atg7, LC3B-Alex488, and ATP, or LC3B-Alex488 alone as a control. We incubated the sample at 37°C and followed in real-time LC3B-Alexa488 localization. After 10 min of protein addition, LC3B-Alexa488 was localized to the LDs' surface only in the presence of the lipidation machinery (Figure 5A). In the course of LD binding, we fully bleached the LC3B signal on an LD, and it re-increased but to a lesser extent as at the beginning of the experiment (Figure 5SA, B); this re-increase was likely due to de novo-lipidation. This observation indicates that

Atg3 lipidates LC3B to LDs. To fully show that lipidation occurred, we collected the samples and ran an SDS-PAGE gel. We found that LC3B-I was indeed lipidated into LC3B-II only in the presence of the minimal Atg3 and Atg7 machinery (Figure 5B).

The purified LDs may have other autophagic proteins or factors recruiting LC3-II. Thus, we switched to artificial LDs to have full control over the parameters. We made triolein-in-buffer droplets decorated by PC/PE (7/3). In the reaction chamber, we first introduced Atg7 and ATP only. After 1hr of incubation at 37°C, no signal of LC3 was observed around the droplets (Figure 5C). We then added Atg3 in the chamber and observed rings of LC3-Alexa488 around some of the droplets (Figure 5C). The presence of all the lipidation machinery from the beginning led to LC3 lipidation to the droplets after few minutes (Figure S5C). We next collected the artificial LDs, analyzed them by SDS-PAGE gel, and found LC3-II only in the presence of the lipidation machinery (Figure 5D).

To study the impact of PC/PE on lipidation, we prepared artificial LDs made of PC/PE (7/3) but with different monolayer phospholipid densities, as in Figure 4C, varied from 0.005% to 0.2% (w/w to triolein). We used LC3B-Alexa647 and Atg3/Atg3-YFP (80/20) to correlate LC3B lipidation to Atg3 binding in the presence of Atg7 and ATP. We observed that only artificial LDs positive for Atg3 were LC3-lipidated (Figure 5E, Figure S5D). Atg3 binding is prevented by a high phospholipid monolayer coverage (Figure 4). We thus used Rho-PE as a proxy for the phospholipid density (Figure 5F) and looked at lipidated LC3B-Alexa488 in the presence of Atg3, Atg7, and ATP. Accordingly, we found that the lipidated droplets had a lower Rh-DOPE signal (Figure 5F, G, and Figure S5E), as they allow more Atg3 binding. These results show that Atg3 LD binding was required for LC3B lipidation, and binding improved on phospholipid-depleted LDs.

Finally, membrane-bound Atg3 can lipidate GABARAPL (Nath et al., 2014). In cells, we did not detect GABARAPs on the large LDs (Figure S1G). In vitro, with both fluorescence imaging and SDS-PAGE gel analysis, we found that Atg3 mediated the lipidation of GABARAP1L to the surface of model LDs (Figure S5F-I). Therefore, in mammalian cells, regulatory factors differentially modulate the localization and function of Atg8 proteins on LDs.

In conclusion, our reconstitution approaches strongly support that Atg3 is recruited to specific LDs' surfaces where it lipidates Atg8 proteins to PE.

LDs mediate LC3 lipidation in the autophagy-deficient DU145 prostate cancer cells

Our data support that the LD surface can serve for LC3B lipidation in mammals by the sole action of Atg3,7. To further test this hypothesis and its implications, we sought to work with autophagy-deficient cells. We chose the DU145 prostate cancer cells, which have alternative transcripts ATG5, lack one or two exons, leading to the premature ending of ATG5 translation and causing a genetically impaired autophagy (Ouyang et al., 2013). Under nutrient starvation conditions, LC3 is not lipidated in these cells unless transfected with Atg5 (Ouyang et al., 2013). The impact of LD accumulation in DU145 on LC3 lipidation is unknown. If our hypothesis is correct, the accumulation of LDs should facilitate LC3 lipidation. In such eventuality, the DU145 cells represent a good model system to get insights into the biological function of the LC3-positive LDs.

DU145 cells were loaded or not with OA for 24h to induce LDs. For each condition, the cells were incubated with EBSS or maintained in complete media. For comparison, we had in parallel Huh7 cells under the same conditions in the OA loading case (Figure 6A). We recovered the lysate and LD fractions and did Western blots. We did not detect ATG5 or LC3-II in the DU145 cell lysates in fed and EBSS conditions (Figure 6A). In the LD fraction, we surprisingly detected LC3B-I, as in Figures 1 and 2. However, we also observed the presence of LC3B-II in the LD fraction during nutrient starvation in EBSS, even in the non-OA loaded condition but to a lower extent; OA loading led to higher levels of both LC3B-I and II in the LD fraction. Compared with Huh7 cells, the level of LC3B-II on the LD fraction was lower. These results indicate that, despite the lack of Atg5, LC3B lipidation happens in DU145 cells, but such reaction is LD dependent. Because of the low lipidation level, LC3B-II is not well detected in cell lysates, given that it concentrates on LDs.

We wanted to confirm by fluorescence imaging the LD localization of LC3B. We transected the DU145 cells with the eGFP-LC3B adenovirus and cultured them in full media or EBSS for 48h. Mainly during nutrient starvation (Figure S6A, S6B), we observed that LC3B localized around LDs. Interestingly, there was almost systematically LC3B puncta in close apposition to the LDs (Figure S6A), reminiscent of the membrane structures seen near 3T3 adipocyte LDs (Figure 1A, Figure S1C, S1D). The possible copurification of these puncta with LDs could explain the presence of the LC3B-I signal in our Western blots (Figure 1, 2, 6).

Altogether, our data with DU145 indicate that LDs enhance the lipidation of LC3B. Whether such functions are related to any autophagic process was unclear. Therefore, we asked if an autophagic flux exists in these cells and how LDs would impact it. By Western blot analysis, we found higher levels of P62 when the cells were loaded with OA (Figure 6B). When they were subsequently incubated with EBSS, the P62 signal dropped (Figure 6B), indicating the

establishment of autophagic flux. Next, we employed the eGFP-mCherry-LC3B reporter for monitoring degradation (Klionsky et al., 2021). In a non-acidified milieu, eGFP and mCherry colocalize. The occurrence of degradation by lysosomes, indicative of autophagic flux, is reported the extinction of the eGFP signal (Kimura et al., 2007). We observed that eGFP and mCherry reporters colocalized on LDs in the DU145 cells at 48hr in EBSS (Figure 6C). However, we also observed many cases where the mCherry was alone, covering LipiTox-positive structures that are likely LD being degraded (Figure 6C). This data shows that LC-3-positive LDs are involved in establishing an autophagic flux in DU145 cells that lack the canonical autophagy pathway.

Large LC3B-positive LDs interact with acidified autophagosome-like membranes

To get insights on LC3B-positive LDs' fate in 3T3 adipocytes, we analyzed the contact between LC3B-positive LDs and LC3B-positive membranes (Figure 7A). In 85% of the analyzed cases, LC3B-positive LDs were associated with LC3B-membranes (Figure 7B). We conducted FRAP experiments on the freestanding LDs' surface vs. their membrane contact regions (Figure 7C and S7A). We obtained different recovery rates: fast for the freestanding LD region and much slower on the contact (Figure 7D and S7B, C). The slowdown of diffusion at the contact likely pertains to the interaction of LC3B between the membrane and the LDs. The diffusive LD LC3B-II pool might be recruited to expand the contact of the LD with the autophagosome-like membrane. Based on LC3-LC3 trans-dimerization capacity (Motta et al., 2018; Nakatogawa et al., 2007), we surmise that LD-LC3B interacts with LC3B on the autophagosome-like structure.

Next, we studied whether the large LDs undergo degradation. In lipophagy, LDs are fully encapsulated by autophagosomes that subsequently fuse with lysosomes, forming the acidified autolysosomes (Liu and Czaja, 2013). When the 3T3 adipocytes were maintained in EBSS for 48h, the large LC3B-positive LDs showed, as above, a faint LC3B surface signal, likely the freely diffusive LC3B-II (Figure 7E); this region was however negative for the lysotracker, excluding that degradation was going on this area of the LD. Instead, the LD region in contact with the LC3B-positive autophagosome-like membrane was positive for the lysotracker (Figure 7E). This area of the LD was probably undergoing degradation while the LD was not entirely encapsulated. When we treated the cells with chloroquine to block autophagosome-lysosome fusion, LC3B-positive membranes still interacted with the LDs, but they were much less acidified (Figure S7D). These observations suggest that lysosomes fused with the LC3B-membranes that are interacting with the LC3B-positive LDs. Such a process is distinct from the classical view of lipophagy and could be essential for the local degradation of LD proteins and neutral lipids (Kaushik and Cuervo, 2015; Schulze et al., 2020).

Whether the LD-autophagosome interaction was a transient step, i.e., before the large LD gets fully encapsulated, was unclear. To test this, we switched to Huh7 cells, which can have large LDs but not as big as those in the 3T3 adipocytes. We noticed similar features in 3T3 cells: a large LD with a clear LC3B signal, negative for the lysotracker, and interacting with acidified LC3-membranes (Figure 7F). We followed this LC3B-positive LD, and its contact with the acidified only modestly increased within a time course of 40min (Figure S7E). This result indicates that the complete wrapping of large LDs would take a much longer time if such happens in the 3T3 cells.

Altogether, our above data support the occurrence of a pathway wherein acidified autophagosome-like structures interact with large LDs to degrade both proteins and lipids from the LD surface potentially. Such degradation process might be specific to adipocytes which bear large LDs in contrast to other cell lines. Finally, LC3B-II might be both the ligand and receptor mediating LD-autophagosome contact.

Discussion.

The cargo size in macroautophagy is in the micrometer range (Klionsky and Eskelinen, 2014; Yim and Mizushima, 2020). Therefore, the localization of LC3B to the few large LDs during long-term nutrient deprivation in EBSS must be different from autophagosomes' signal. Our data support that LC3B is directly lipidated to the surface of these LDs by the minimal Atg3 and Atg7 machinery. This preference for big LDs is not due to LD curvature as, in vitro, ATG3 lipidated LC3B to both sonicated and macroscopic droplets (Figure 4).

Atg3 binds to model LDs and only to the most highly curved bilayers, likely because both LDs and curved membranes exhibit relatively sparse lipid packing (Antonny, 2011; Chorlay and Thiam, 2020). This probably explains why the recruitment of Atg3 to bilayers in cells ordinarily requires additional machinery, including the Atg5-Atg12-Atg16 complex. In vitro, Atg3 LD recruitment is enhanced by PE, suggesting that large LDs might bear more PE, consistent with in vitro biophysical studies (Ben M'barek et al., 2017). When cells are exposed to EBSS for a long-term period, the monolayer of large LDs may get even more enriched in specific lipids, e.g., PE, and decreased in packing, e.g., by the remodeling of their surface proteome and lipidome. Such a surface remodeling would trigger Atg3 binding and LC3B lipidation.

DU145 prostate cancer cells are deficient in autophagy. Therefore, it is remarkable to observe that OA's simple induction of LDs rescued LC3B lipidation and enhanced autophagic fluxes (Figure 6). Thus, LDs' surface may directly support autophagy biogenesis and function, especially in this cell line. More generally, a tempting model is that during long-term nutrient deprivation, the classical autophagy pathway is overwhelmed and autophagic processes become more easily organized at the surface of some LDs to alleviate the system.

In 3T3 adipocyte and Huh7 cells, LC3B-positive membranes adhered to the LC3B-positive LDs (Figure 7C, F). Considering the capacity of Atg8 proteins to trans-dimerize (Motta et al., 2018; Nakatogawa et al., 2007), LC3-LC3 trans-interaction could promote the docking of the autophagosome-like membranes to the LDs. Thereupon, LC3 might be an adaptor on LD mediating the interaction with autophagosomes, such as in lipophagy. Intriguingly, the autophagosome-like structures fused with lysosomes while the LDs were not fully engulfed (Figure 7E, F). This sequence of events is different from the classical view of lipophagy, where LDs are fully engulfed before being delivered to lysosomes (Liu and Czaja, 2013; Singh et al., 2009). Therefore, the topology we identified here seems unique in mediating LD degradation, occurring only on the large LC3B-positive LDs. LDs that undergo classical lipophagy, usually smaller, might use other protein adaptors to interact with autophagosomes, e.g., Rab10 (Li et al., 2016).

Prior to our work, several autophagic proteins have been reported to bind to the surface of LDs, including Atg2, Atg14, and DFCP1 (Gao et al., 2019; Li et al., 2019; Pfisterer et al., 2014; Shibata et al., 2009, 2010; Velikkakath et al., 2012). These findings first agree that autophagic processes, as we found here, can directly take place at LD's surface for degradation. Secondly, together with our data, the findings support the model that the LD surface might support autophagosome biogenesis, likely at ER-autophagosome-LD connections. In this view, the LD surface could serve as an LC3B lipidation platform, generates LC3B-II, which could diffuse to nascent autophagosomes via bridges established with the ER.

In conclusion, our data reveal a non-conventional LC3B function at the surface of LDs and highlights a direct relationship between autophagy and LDs. In particular, our findings in DU145 cells point to the physiological importance of LDs in diseases through cross-talking to autophagy.

REFERENCES

Ajjaji, D., Ben M'barek, K., Mimmack, M.L., England, C., Herscovitz, H., Dong, L., Kay, R.G., Patel, S., Saudek, V., and Small, D.M. (2019). Dual binding motifs underpin the hierarchical association of perilipins1–3 with lipid droplets. Mol. Biol. Cell *30*, 703–716.

Antonny, B. (2011). Mechanisms of membrane curvature sensing. Annu. Rev. Biochem. *80*, 101–123.

Ben M'barek, K., Ajjaji, D., Chorlay, A., Vanni, S., Forêt, L., and Thiam, A.R. (2017). ER Membrane Phospholipids and Surface Tension Control Cellular Lipid Droplet Formation. Dev. Cell *41*, 591-604.e7.

Caillon, L., Nieto, V., Gehan, P., Omrane, M., Rodriguez, N., Monticelli, L., and Thiam, A.R. (2020). Triacylglycerols sequester monotopic membrane proteins to lipid droplets. Nat. Commun. *11*, 1–12.

Chorlay, A., and Thiam, A.R. (2020). Neutral lipids regulate amphipathic helix affinity for model lipid droplets. J. Cell Biol. *219*.

Chorlay, A., Santinho, A., and Thiam, A.R. (2020). Making Droplet-Embedded Vesicles to Model Cellular Lipid Droplets. STAR Protoc. 100116.

Dhiman, R., Caesar, S., Thiam, A.R., and Schrul, B. (2020). Mechanisms of protein targeting to lipid droplets: A unified cell biological and biophysical perspective. In Seminars in Cell & Developmental Biology, (Elsevier), p.

Dooley, H.C., Razi, M., Polson, H.E., Girardin, S.E., Wilson, M.I., and Tooze, S.A. (2014). WIPI2 links LC3 conjugation with PI3P, autophagosome formation, and pathogen clearance by recruiting Atg12–5-16L1. Mol. Cell *55*, 238–252.

Dupont, N., Chauhan, S., Arko-Mensah, J., Castillo, E.F., Masedunskas, A., Weigert, R., Robenek, H., Proikas-Cezanne, T., and Deretic, V. (2014). Neutral lipid stores and lipase PNPLA5 contribute to autophagosome biogenesis. Curr. Biol. *24*, 609–620.

Feng, Y., He, D., Yao, Z., and Klionsky, D.J. (2014). The machinery of macroautophagy. Cell Res. *24*, 24–41.

Galluzzi, L., and Green, D.R. (2019). Autophagy-independent functions of the autophagy machinery. Cell *177*, 1682–1699.

Gammoh, N., Florey, O., Overholtzer, M., and Jiang, X. (2013). Interaction between FIP200 and ATG16L1 distinguishes ULK1 complex–dependent and–independent autophagy. Nat. Struct. Mol. Biol. *20*, 144.

Gao, G., Sheng, Y., Yang, H., Chua, B.T., and Xu, L. (2019). DFCP1 associates with lipid droplets. Cell Biol. Int. *43*, 1492–1504.

Gatica, D., Lahiri, V., and Klionsky, D.J. (2018). Cargo recognition and degradation by selective autophagy. Nat. Cell Biol. *20*, 233–242.

Heckmann, B.L., and Green, D.R. (2019). LC3-associated phagocytosis at a glance. J. Cell Sci. *132*.

546 Herb, M., Gluschko, A., and Schramm, M. (2020). LC3-associated phagocytosis-the highway
547 to hell for phagocytosed microbes. In Seminars in Cell & Developmental Biology, (Elsevier),
548 pp. 68–76.

549 Ichimura, Y., Kirisako, T., Takao, T., Satomi, Y., Shimonishi, Y., Ishihara, N., Mizushima,
550 N., Tanida, I., Kominami, E., Ohsumi, M., et al. (2000). A ubiquitin-like system mediates
551 protein lipidation. Nature *408*, 488–492.

552 Jin, M., and Klionsky, D.J. (2014). Regulation of autophagy: modulation of the size and
553 number of autophagosomes. FEBS Lett. *588*, 2457–2463.

554 Kaushik, S., and Cuervo, A.M. (2015). Degradation of lipid droplet-associated proteins by
555 chaperone-mediated autophagy facilitates lipolysis. Nat. Cell Biol. *17*, 759–770.

556 Kim, J., Dalton, V.M., Eggerton, K.P., Scott, S.V., and Klionsky, D.J. (1999). Apg7p/Cvt2p
557 Is Required for the Cytoplasm-to-Vacuole Targeting, Macroautophagy, and Peroxisome
558 Degradation Pathways. Mol. Biol. Cell *10*, 1337–1351.

559 Kimura, S., Noda, T., and Yoshimori, T. (2007). Dissection of the autophagosome maturation
560 process by a novel reporter protein, tandem fluorescent-tagged LC3. Autophagy *3*, 452–460.

561 Klionsky, D.J., and Eskelinen, E.-L. (2014). The vacuole vs. the lysosome: When size
562 matters. Autophagy *10*, 185–187.

563 Klionsky, D.J., Abdel-Aziz, A.K., Abdelfatah, S., Abdellatif, M., Abdoli, A., Abel, S.,
564 Abeliovich, H., Abildgaard, M.H., Abudu, Y.P., and Acevedo-Arozena, A. (2021). Guidelines
565 for the use and interpretation of assays for monitoring autophagy. Autophagy 1–382.

566 Kory, N., Farese Jr, R.V., and Walther, T.C. (2016). Targeting fat: mechanisms of protein
567 localization to lipid droplets. Trends Cell Biol. *26*, 535–546.

568 Lamb, C.A., Dooley, H.C., and Tooze, S.A. (2013). Endocytosis and autophagy: shared
569 machinery for degradation. Bioessays *35*, 34–45.

570 Le Lay, S., Briand, N., Blouin, C.M., Chateau, D., Prado, C., Lasnier, F., Liepvre, X.,
571 Hajduch, E., and Dugail, I. (2010). The lipoatrophic caveolin-1 deficient mouse model reveals
572 autophagy in mature adipocytes. Autophagy *6*, 754–763.

573 Li, D., Song, J.-Z., Li, H., Shan, M.-H., Liang, Y., Zhu, J., and Xie, Z. (2015). Storage lipid
574 synthesis is necessary for autophagy induced by nitrogen starvation. FEBS Lett. *589*, 269–
575 276.

576 Li, D., Zhao, Y.G., Li, D., Zhao, H., Huang, J., Miao, G., Feng, D., Liu, P., Li, D., and Zhang,
577 H. (2019). The ER-localized protein DFCP1 modulates ER-lipid droplet contact formation.
578 Cell Rep. *27*, 343–358.

579 Li, Z., Schulze, R.J., Weller, S.G., Krueger, E.W., Schott, M.B., Zhang, X., Casey, C.A., Liu,
580 J., Stöckli, J., and James, D.E. (2016). A novel Rab10-EHBP1-EHD2 complex essential for
581 the autophagic engulfment of lipid droplets. Sci. Adv. *2*, e1601470.

582 Liu, K., and Czaja, M.J. (2013). Regulation of lipid stores and metabolism by lipophagy. Cell
583 Death Differ. *20*, 3–11.

584 Liu, J., Xia, H., Kim, M., Xu, L., Li, Y., Zhang, L., Cai, Y., Norberg, H.V., Zhang, T., and
585 Furuya, T. (2011). Beclin1 controls the levels of p53 by regulating the deubiquitination
586 activity of USP10 and USP13. Cell *147*, 223–234.

587 Martens, S., and Fracchiolla, D. (2020). Activation and targeting of ATG8 protein lipidation.
588 Cell Discov. *6*, 1–11.

589 Martinez, J., Almendinger, J., Oberst, A., Ness, R., Dillon, C.P., Fitzgerald, P., Hengartner,
590 M.O., and Green, D.R. (2011). Microtubule-associated protein 1 light chain 3 alpha (LC3)-
591 associated phagocytosis is required for the efficient clearance of dead cells. Proc. Natl. Acad.
592 Sci. *108*, 17396–17401.

593 Martinez-Lopez, N., Garcia-Macia, M., Sahu, S., Athonvarangkul, D., Liebling, E., Merlo, P.,
594 Cecconi, F., Schwartz, G.J., and Singh, R. (2016). Autophagy in the CNS and periphery
595 coordinate lipophagy and lipolysis in the brown adipose tissue and liver. Cell Metab. *23*, 113–
596 127.

597 Melia, T.J., Lystad, A.H., and Simonsen, A. (2020). Autophagosome biogenesis: From
598 membrane growth to closure. J. Cell Biol. *219*.

599 Mizushima, N. (2020). The ATG conjugation systems in autophagy. Curr. Opin. Cell Biol.
600 *63*, 1–10.

601 Mizushima, N., and Komatsu, M. (2011). Autophagy: renovation of cells and tissues. Cell
602 *147*, 728–741.

603 Mizushima, N., Ohsumi, Y., and Yoshimori, T. (2002). Autophagosome formation in
604 mammalian cells. Cell Struct. Funct. *27*, 421–429.

605 Mizushima, N., Yoshimori, T., and Ohsumi, Y. (2011). The role of Atg proteins in
606 autophagosome formation. Annu. Rev. Cell Dev. Biol. *27*, 107–132.

607 Motta, I., Nguyen, N., Gardavot, H., Richerson, D., Pincet, F., and Melia, T.J. (2018).
608 GABARAP Like-1 enrichment on membranes: Direct observation of trans-homo-
609 oligomerization between membranes and curvature-dependent partitioning into membrane
610 tubules. BioRxiv 348730.

611 Nakatogawa, H. (2020). Mechanisms governing autophagosome biogenesis. Nat. Rev. Mol.
612 Cell Biol. *21*, 439–458.

613 Nakatogawa, H., Ichimura, Y., and Ohsumi, Y. (2007). Atg8, a ubiquitin-like protein required
614 for autophagosome formation, mediates membrane tethering and hemifusion. Cell *130*, 165–
615 178.

616 Nath, S., Dancourt, J., Shteyn, V., Puente, G., Fong, W.M., Nag, S., Bewersdorf, J.,
617 Yamamoto, A., Antonny, B., and Melia, T.J. (2014). Lipidation of the LC3/GABARAP
618 family of autophagy proteins relies on a membrane-curvature-sensing domain in Atg3. Nat.
619 Cell Biol. *16*, 415.

620 Nguyen, N., Shteyn, V., and Melia, T.J. (2017). Sensing membrane curvature in
621 macroautophagy. J. Mol. Biol. *429*, 457–472.

622 Nishimura, T., Kaizuka, T., Cadwell, K., Sahani, M.H., Saitoh, T., Akira, S., Virgin, H.W.,
623 and Mizushima, N. (2013). FIP200 regulates targeting of Atg16L1 to the isolation membrane.
624 EMBO Rep. *14*, 284–291.

625 Olzmann, J.A., and Carvalho, P. (2018). Dynamics and functions of lipid droplets. Nat. Rev.
626 Mol. Cell Biol. 1.

627 Ouyang, D.-Y., Xu, L.-H., He, X.-H., Zhang, Y.-T., Zeng, L.-H., Cai, J.-Y., and Ren, S.
628 (2013). Autophagy is differentially induced in prostate cancer LNCaP, DU145 and PC-3 cells
629 via distinct splicing profiles of ATG5. Autophagy *9*, 20–32.

630 Pankiv, S., Clausen, T.H., Lamark, T., Brech, A., Bruun, J.-A., Outzen, H., Øvervatn, A.,
631 Bjørkøy, G., and Johansen, T. (2007). p62/SQSTM1 binds directly to Atg8/LC3 to facilitate
632 degradation of ubiquitinated protein aggregates by autophagy. J. Biol. Chem. *282*, 24131–
633 24145.

634 Pfisterer, S.G., Bakula, D., Frickey, T., Cezanne, A., Brigger, D., Tschan, M.P., Robenek, H.,
635 and Proikas-Cezanne, T. (2014). Lipid droplet and early autophagosomal membrane targeting
636 of Atg2A and Atg14L in human tumor cells. J. Lipid Res. *55*, 1267–1278.

637 Sathyanarayan, A., Mashek, M.T., and Mashek, D.G. (2017). ATGL Promotes
638 Autophagy/Lipophagy via SIRT1 to Control Hepatic Lipid Droplet Catabolism. Cell Rep. *19*,
639 1–9.

640 Sawa-Makarska, J., Baumann, V., Coudevylle, N., von Bülow, S., Nogellova, V., Abert, C.,
641 Schuschnig, M., Graef, M., Hummer, G., and Martens, S. (2020). Reconstitution of
642 autophagosome nucleation defines Atg9 vesicles as seeds for membrane formation. Science
643 *369*.

644 Schott, M.B., Weller, S.G., Schulze, R.J., Krueger, E.W., Drizyte-Miller, K., Casey, C.A., and
645 McNiven, M.A. (2019). Lipid droplet size directs lipolysis and lipophagy catabolism in
646 hepatocytes. J. Cell Biol. *218*, 3320–3335.

647 Schulze, R.J., Krueger, E.W., Weller, S.G., Johnson, K.M., Casey, C.A., Schott, M.B., and
648 McNiven, M.A. (2020). Direct lysosome-based autophagy of lipid droplets in hepatocytes.
649 Proc. Natl. Acad. Sci.

650 Schütter, M., Giavalisco, P., Brodesser, S., and Graef, M. (2020). Local fatty acid channeling
651 into phospholipid synthesis drives phagophore expansion during autophagy. Cell *180*, 135–
652 149.

653 Shibata, M., Yoshimura, K., Furuya, N., Koike, M., Ueno, T., Komatsu, M., Arai, H., Tanaka,
654 K., Kominami, E., and Uchiyama, Y. (2009). The MAP1-LC3 conjugation system is involved
655 in lipid droplet formation. Biochem. Biophys. Res. Commun. *382*, 419–423.

656 Shibata, M., Yoshimura, K., Tamura, H., Ueno, T., Nishimura, T., Inoue, T., Sasaki, M.,
657 Koike, M., Arai, H., and Kominami, E. (2010). LC3, a microtubule-associated protein1A/B
658 light chain3, is involved in cytoplasmic lipid droplet formation. Biochem. Biophys. Res.
659 Commun. *393*, 274–279.

660 Shpilka, T., Welter, E., Borovsky, N., Amar, N., Mari, M., Reggiori, F., and Elazar, Z. (2015).
661 Lipid droplets and their component triglycerides and steryl esters regulate autophagosome
662 biogenesis. EMBO J. *34*, 2117–2131.

663 Singh, R., and Cuervo, A.M. (2012). Lipophagy: connecting autophagy and lipid metabolism.
664 Int. J. Cell Biol. *2012*.

665 Singh, R., Kaushik, S., Wang, Y., Xiang, Y., Novak, I., Komatsu, M., Tanaka, K., Cuervo,
666 A.M., and Czaja, M.J. (2009). Autophagy regulates lipid metabolism. Nature *458*, 1131–
667 1135.

668 Small, D.M., Wang, L., and Mitsche, M.A. (2009). The adsorption of biological peptides and
669 proteins at the oil/water interface. A potentially important but largely unexplored field. J.
670 Lipid Res. *50*, S329–S334.

671 Thiam, A.R., and Dugail, I. (2019). Lipid droplet–membrane contact sites–from protein
672 binding to function. J. Cell Sci. *132*, jcs230169.

673 Thiam, A.R., Farese Jr, R.V., and Walther, T.C. (2013). The biophysics and cell biology of
674 lipid droplets. Nat. Rev. Mol. Cell Biol. *14*, 775.

675 Thukral, L., Sengupta, D., Ramkumar, A., Murthy, D., Agrawal, N., and Gokhale, R.S.
676 (2015). The Molecular Mechanism Underlying Recruitment and Insertion of Lipid-Anchored
677 LC3 Protein into Membranes. Biophys. J. *109*, 2067–2078.

678 Velázquez, A.P., Tatsuta, T., Ghillebert, R., Drescher, I., and Graef, M. (2016). Lipid droplet–
679 mediated ER homeostasis regulates autophagy and cell survival during starvation. J. Cell
680 Biol. *212*, 621–631.

681 Velikkakath, A.K.G., Nishimura, T., Oita, E., Ishihara, N., and Mizushima, N. (2012).
682 Mammalian Atg2 proteins are essential for autophagosome formation and important for
683 regulation of size and distribution of lipid droplets. Mol. Biol. Cell *23*, 896–909.

684 Welte, M.A., and Gould, A.P. (2017). Lipid droplet functions beyond energy storage.
685 Biochim. Biophys. Acta Mol. Cell Biol. Lipids *1862*, 1260–1272.

686 Wolins, N.E., Brasaemle, D.L., and Bickel, P.E. (2006). A proposed model of fat packaging
687 by exchangeable lipid droplet proteins. FEBS Lett. *580*, 5484–5491.

688 Yim, W.W.-Y., and Mizushima, N. (2020). Lysosome biology in autophagy. Cell Discov. *6*,
689 1–12.

690

691

692

ACKNOWLEDGMENTS

We are thankful to all the group members for their valuable comments and critical read of the manuscript. This work was supported by the Programme Emergence de la Ville de Paris (DDEEES 165), the Fondation pour la Recherche Médicale (FRM : EQU202103012564), the ANR-16-TERC-0002-01 (LDEN) to ART.

Competing interests

The authors declare no competing interests.

Author contributions

The research was designed by MO, KBM, TM, and ART. MO, KBM, and AS performed all experiments. SN and NG prepared all proteins used in vitro. ART wrote the manuscript, reviewed by all co-authors.

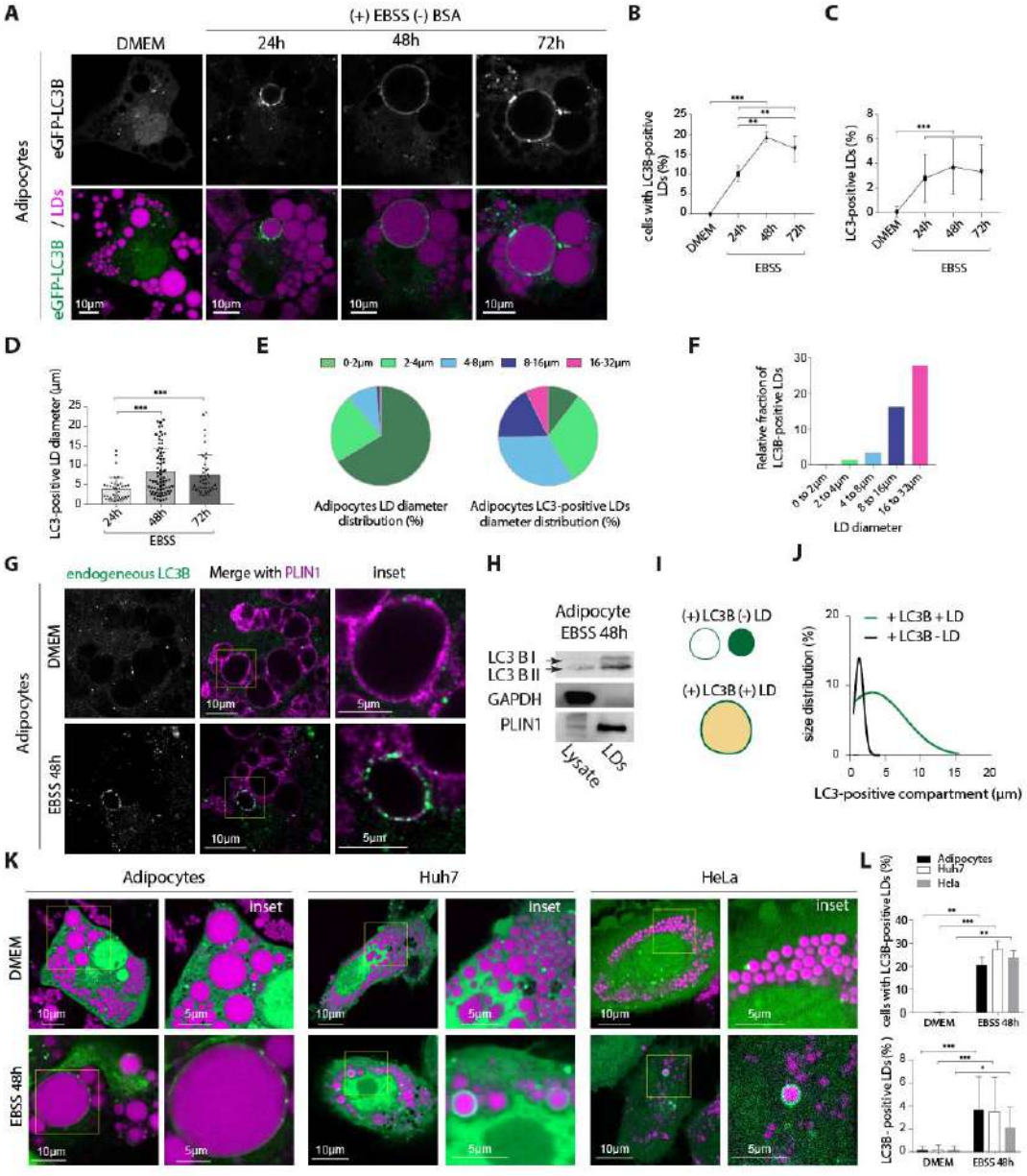
A
(+) EBSS (-) BSA
DMEM
24h
48h
72h
Adipocytes
eGFP-LC3B
/ LDs
eGFP-LC3B
10µm
B
cells with LC3B-positive LDs (%)
DMEM
24h
48h
72h
EBSS
C
LC3-positive LDs (%)
DMEM
24h
48h
72h
EBSS
D
LC3-positive LD diameter (µm)
24h
48h
72h
EBSS
E
0-2µm
2-4µm
4-8µm
8-16µm
16-32µm
Adipocytes LD diameter distribution (%)
Adipocytes LC3-positive LDs diameter distribution (%)
F
Relative fraction of LC3B-positive LDs
0 to 2µm
2 to 4µm
4 to 8µm
8 to 16µm
16 to 32µm
LD diameter
G
endogeneous LC3B
Merge with PLIN1
Inset
Adipocytes
DMEM
EBSS 48h
10µm
5µm
H
Adipocyte
EBSS 48h
LC3 B I
LC3 B II
GAPDH
PLIN1
Lysate
LDs
I
(+) LC3B (-) LD
(+) LC3B (+) LD
J
+ LC3B + LD
+ LC3B - LD
size distribution (%)
LC3-positive compartment (µm)
K
Adipocytes
Huh7
HeLa
Inset
DMEM
EBSS 48h
10µm
5µm
L
Adipocytes
Huh7
Hela
cells with LC3B-positive LDs (%)
LC3B - positive LDs (%)
DMEM
EBSS 48h

Figure 1

710

Figure 1. LC3B is recruited to LDs during long-term nutrient deprivation

A. Confocal imaging of eGFP-LC3B and LDs in differentiated 3T3 L1 adipocytes, virally transfected with eGFP-LC3B. Cells were incubated in EBSS for the indicated time after transfection. Scale bar, 10 μm.

B. Percentage of cells with eGFP-LC3B-positive LDs. Data were obtained from three independent experiments done as described in A. Ordinary one-way ANOVA test was used (** P < 0.01, *** P<0.0001).

C. Percentage of eGFP-LC3B-positive LDs per cell. Data were obtained from three independent experiments done as described in A. ordinary one-way ANOVA test was used (*** P<0.0001).

D. Diameter of eGFP-LC3B-positive LDs quantified from three independent experiments done as described in A. Ordinary one-way ANOVA test was used (*** P<0.0001).

E. Left: sector graph shows the size distribution of LDs in differentiated 3T3L1 adipocytes, transfected with eGFP-LC3B and incubated in EBSS for 48hs. Three independent experiments n=10 cells were collapsed. The right sector graph shows the size distribution of eGFP-LC3B-positive LDs. Quantifications are from 4 independent experiments.

F. Percentage of eGFP-LC3B-positive LDs in a size range, representing another representation of E.

G. Immunofluorescence staining of LC3B and PLIN1 in differentiated 3T3 L1 adipocytes incubated in EBSS for 48hs.

H. Western blot of lysate and LDs fractions of cells treated as described in G.

I. Schematic representation of LC3 puncta with or without LD.

J. Puncta size distribution with or without LDs; from 10 cells from three independent experiments.

K. Confocal imaging of eGFP-LC3B and LDs in differentiated 3t3 L1 adipocytes, Hela and Huh7 cells. Adipocytes, HeLa, and Huh7 cells were treated with OA to induce LD formation for 24hs and then incubated in EBSS for 48hs after transfection. Scale bar,10 μm (5 μm in insets).

L. Top panel: Percentage of cells with eGFP-LC3B-positive LDs, from three independent experiments done as described in K. Student's unpaired t-test is used for each cell line (*** P<0,0001), (** P<0,001). Bottom panel: percentage of eGFP-LC3B-positive LDs per cell. Data are from three independent experiments done as described in K. Student's unpaired t-test is used (*** P<0,0001), (** P<0,001).

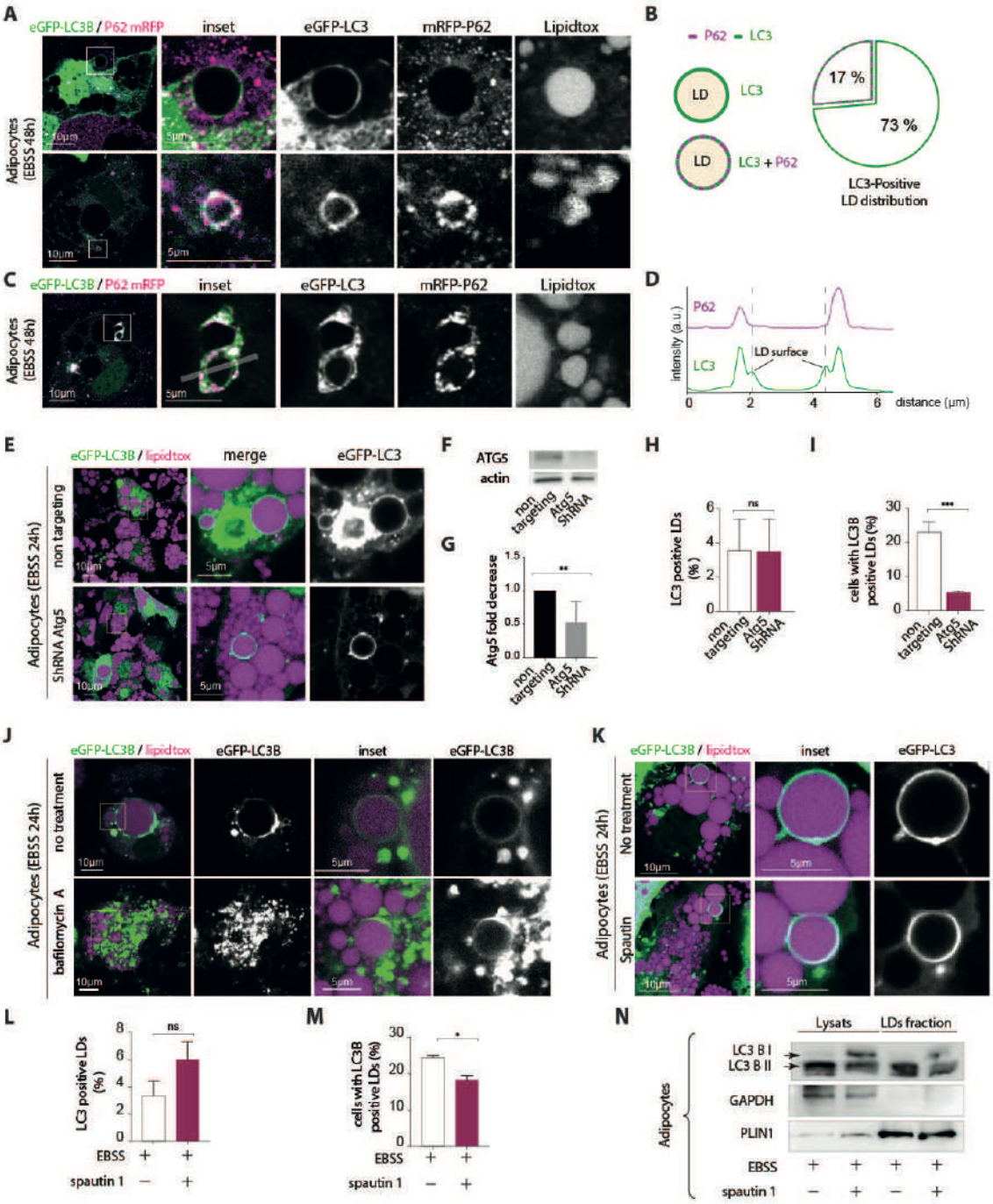
A
eGFP-LC3B / P62 mRFP
inset
eGFP-LC3
mRFP-P62
Lipidtox
Adipocytes (EBSS 48h)
B
P62
LC3
LD
LC3
LD
LC3 + P62
17 %
73 %
LC3-Positive LD distribution
C
eGFP-LC3B / P62 mRFP
inset
eGFP-LC3
mRFP-P62
Lipidtox
Adipocytes (EBSS 48h)
D
P62
LC3
LD surface
intensity (a.u.)
distance (µm)
E
eGFP-LC3B / lipidtox
merge
eGFP-LC3
Adipocytes (EBSS 24h)
non targeting
shRNA Atg5
F
ATG5
actin
non targeting
Atg5 ShRNA
G
Atg5 fold decrease
H
LC3 positive LDs (%)
ns
I
cells with LC3B positive LDs (%)
J
eGFP-LC3B / lipidtox
eGFP-LC3B
inset
Adipocytes (EBSS 24h)
no treatment
bafilomycin A
K
eGFP-LC3B / lipidtox
inset
eGFP-LC3
Adipocytes (EBSS 24h)
No treatment
Spautin
L
LC3 positive LDs (%)
ns
EBSS
spautin 1
M
cells with LC3B positive LDs (%)
EBSS
spautin 1
N
Lysats
LDs fraction
LC3 B I
LC3 B II
GAPDH
PLIN1
Adipocytes
EBSS
spautin 1

Figure 2

Figure 2. LC3B is not recruited to LDs by known factors

A. Confocal imaging of eGFP-LC3B, P62-mRFP and LDs in differentiated 3T3 L1 adipocytes. The cells were virally transfected with eGFP-LC3B and P62-mRFP and incubated in EBSS for 48hs. Scale bar,10 µm (5 µm in insets).
B. Left: schematic representation illustrating the recruitment of eGFP-LC3B alone or with P62-mRFP on LDs. Right: sector graph showing the percentage of LDs in which eGFP-LC3B is recruited alone or with P62-mRFP on LDs. Quantifications are from three independent experiments.
C. Confocal imaging of differentiated 3T3 L1 adipocytes. An example of a colocalization between eGFP and P62 near an LC3-positve LD. Scale bar,10 µm (5 µm in insets).
D. Line profile showing the color intensity profile of eGFP-LC3B , P62-mRFP for the line drawn in the inset image of panel C.
E. Confocal imaging of LDs in differentiated 3T3 L1 adipocytes virally co-transfected with eGFP-LC3B and an ATG5 shRNA or the non-targeting shRNA. Scale bar,10 µm (5 µm in insets).
F. Western blot of cells treated as described in E.
G. Quantitation of three Western blot experiments of cells treated as described in E.
H. Percentage of eGFP-LC3B-positive LDs per cell. Quantifications are from three independent experiments. Student's unpaired t-test is used (ns P>0,05)
I. Percentage of cells with eGFP-LC3B-positive LDs. Quantifications are from three independent experiments. Student's unpaired t-test is used (*** P<0,0001)
J. Confocal imaging of eGFP-LC3B and LDs in differentiated 3T3 L1 adipocytes virally transfected with eGFP-LC3B and incubated in EBSS alone or EBSS containing bafilomycin A for 48hs. Scale bar,10 µm (5 µm in insets).
K. Confocal imaging of eGFP-LC3B and LDs in differentiated 3T3 L1 adipocytes virally transfected with eGFP-LC3B and incubated in EBSS alone or EBSS containing spautin 1 for 48hs. Scale bar,10 µm (5 µm in insets).
L. Percentage of eGFP-LC3B-positive LDs in the cell. Quantifications are from three independent experiments. Student's unpaired t-test is used (ns P>0,05)
M. Percentage of cells with eGFP-LC3B-positive LDs. Quantifications are from three independent experiments. Student's unpaired t-test is used (* P<0,05)
N. Western blot of lysate and LD fractions of differentiated adipocytes incubated in EBSS alone or EBSS containing spautin 1 for 48hs.

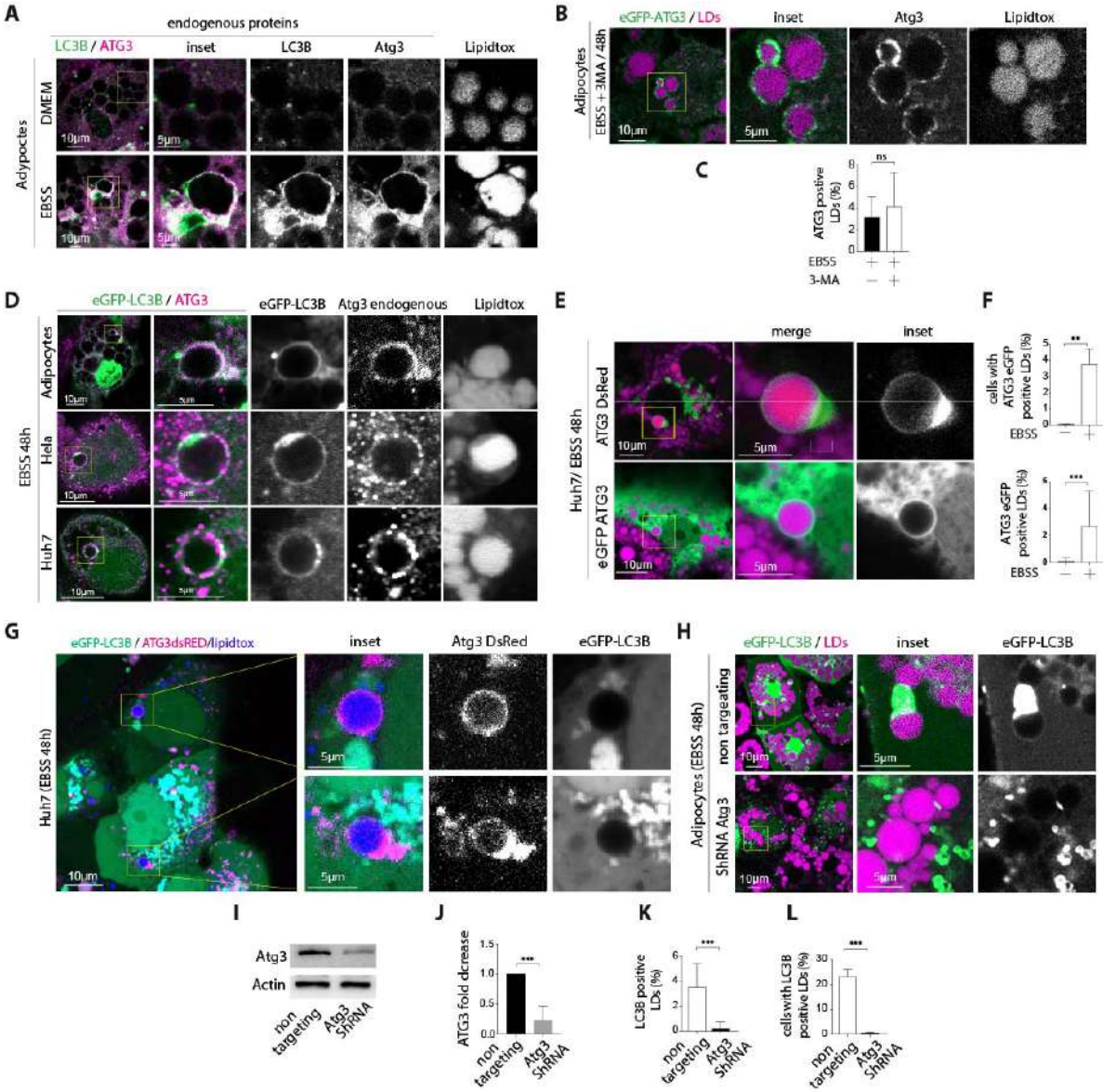
A
endogenous proteins
LC3B / ATG3
inset
LC3B
Atg3
Lipidtox
Adypoctes
DMEM
EBSS
B
eGFP-ATG3 / LDs
inset
Atg3
Lipidtox
Adipocytes
EBSS + 3MA / 48h
C
ATG3 positive LDs (%)
ns
EBSS
3-MA
D
eGFP-LC3B / ATG3
eGFP-LC3B
Atg3 endogenous
Lipidtox
EBSS 48h
Adipocytes
Hela
Huh7
E
merge
inset
Huh7/ EBSS 48h
ATG3 DsRed
eGFP ATG3
F
cells with ATG3 eGFP positive LDs (%)
ATG3 eGFP positive LDs (%)
EBSS
G
eGFP-LC3B / ATG3dsRED/lipidtox
inset
Atg3 DsRed
eGFP-LC3B
Huh7 (EBSS 48h)
H
eGFP-LC3B / LDs
inset
eGFP-LC3B
Adipocytes (EBSS 48h)
non targeating
ShRNA Atg3
I
Atg3
Actin
non targeting
Atg3 ShRNA
J
ATG3 fold dcrease
K
LC3B positive LDs (%)
L
cells with LC3B positive LDs (%)

Figure 3

Figure 3. ATG3 is recruited to the lipid droplet surface during long-term nutrient starvation

A. Immuno-fluorescence staining of LC3B, ATG3 and LDs in differentiated 3T3 L1 adipocytes incubated in DMEM, EBSS or EBSS containing 3MA for 48hs.
B. Immuno-fluorescence staining of ATG3 and LDs in differentiated 3T3 L1 adipocytes incubated in EBSS containing 3MA for 48hs.
C. Percentage of ATG3-positive LDs per cell. n= 10 cells Student's unpaired t-test is used (ns P>0,05).
D. Immuno-fluorescence staining of ATG3 and LDs in differentiated 3T3 L1 adipocytes, Huh7 and Hela cells transfected with eGFP-LC3B and incubated in EBSS for 48hs.
E. Confocal imaging of Huh7 cells transfected with eGFP-ATG3 or ATG3-dsRED. Cells are treated with OA to induce LDs and then incubated in EBSS for 48hs.
F. Percentage of cells with eGFP-ATG3-positive LDs (top) and of eGFP-ATG3-positive LDs per cell (bottom). Quantifications are from three independent experiments. Student's unpaired t-test is used (** P<0,001), (*** P<0,0001).
G. Confocal imaging of Huh7 cells co-transfected with EGFP-LC3B and ATG3-dsRED. Cells are treated with OA to induce LDs and then incubated in EBSS for 48hs.
H. Confocal imaging of LDs in differentiated 3T3 L1 adipocytes virally co-transfected with eGFP-LC3B and an ATG3 shRNA or eGFP-LC3B and the non-targeting shRNA. Cells are incubated in EBSS for 48hs after transfection. Scale bar, 10 μm (5 μm in insets).
I. Western blot of cells treated as described in H.
J. Bar graph shows the quantification of three Western blot experiments of cells treated as described in H.
K. Percentage of eGFP-LC3B-positive LDs per cell. Quantifications are from three independent experiments. Student's unpaired t-test is used (*** P<0,0001)
L. Percentage of cells with eGFP-LC3B-positive LDs. Quantifications are from three independent experiments. Student's unpaired t-test is used (*** P<0,0001).

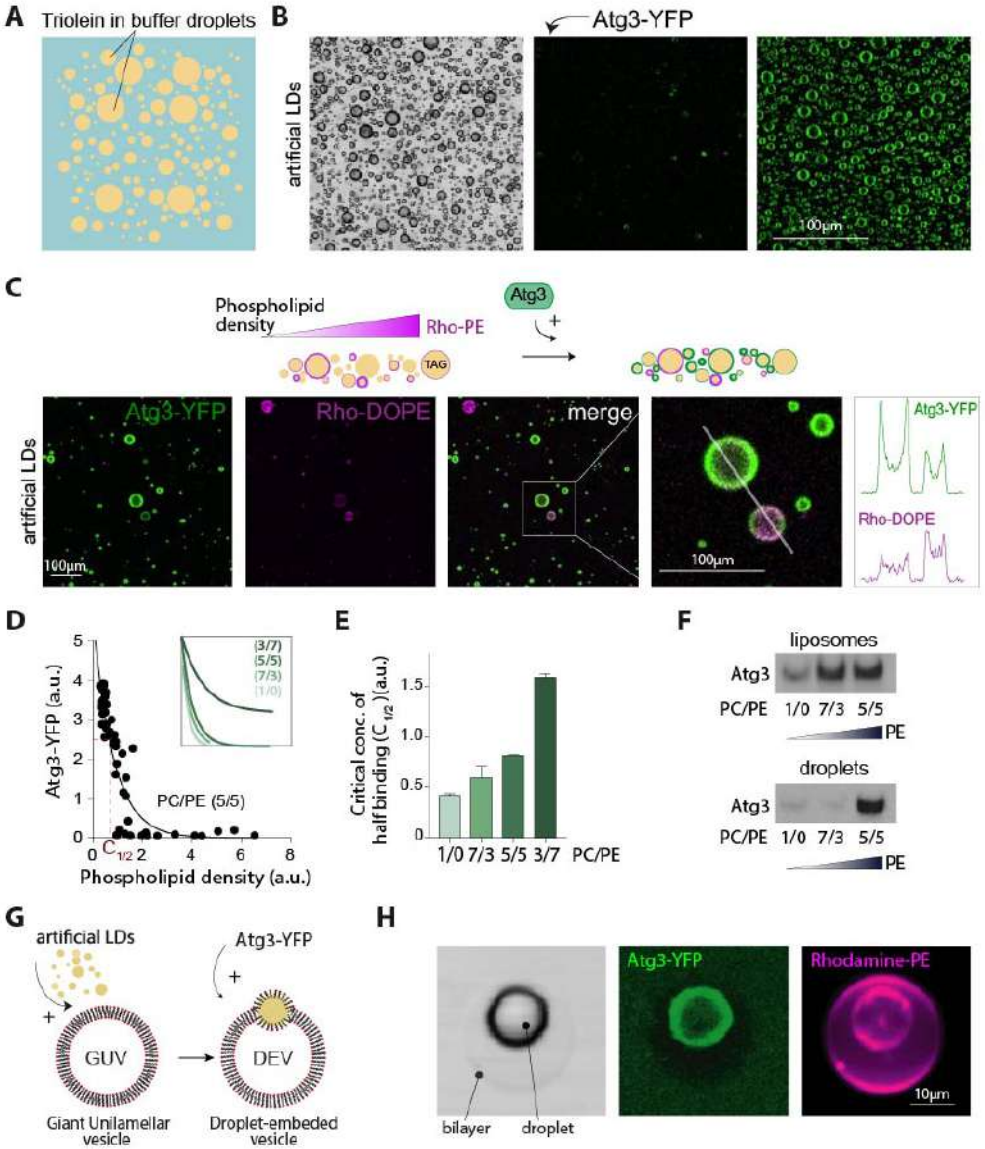
A
Triolein in buffer droplets
B
Atg3-YFP
artificial LDs
100µm
C
Phospholipid density
Rho-PE
Atg3
TAG
Atg3-YFP
Rho-DOPE
merge
artificial LDs
100µm
100µm
Atg3-YFP
Rho-DOPE
D
Atg3-YFP (a.u.)
(3/7)
(5/5)
(7/3)
(1/0)
PC/PE (5/5)
C1/2
Phospholipid density (a.u.)
E
Critical conc. of half binding (C1/2) (a.u.)
1/0 7/3 5/5 3/7 PC/PE
F
liposomes
Atg3
PC/PE 1/0 7/3 5/5
PE
droplets
Atg3
PC/PE 1/0 7/3 5/5
PE
G
artificial LDs
Atg3-YFP
GUV
DEV
Giant Unilamellar vesicle
Droplet-embeded vesicle
H
Atg3-YFP
Rhodamine-PE
10µm
bilayer
droplet

Figure 4

942

Figure 4. Atg3 better binds to model LDs enriched in PE

A. Schematic representation illustrating triolein droplets made in buffer.
B. Confocal imaging of triolein droplets before and after ATG3-YFP addition.
C. Top: Schematic representation illustrating triolein-in-buffer droplets decorated by different phospholipid levels ((1/1) PC/PE), reported by rhodamine-PE (Rho-PE). Bottom: example confocal imaging of triolein-in-buffer droplets with different phospholipid coverage, ranging from 0.005% to 0.2% (w/w to triolein). Line profiles (left panel) show the intensity levels of ATG3-YFP and Rho-PE on droplets depicted in the inset.
D. ATG3-YFP recruitment to triolein droplets as a function of the phospholipid density, reported by Rho-PE. The concentration at the half of maximum binging is depicted on the main figure. half binding $C_{1/2}$ is shown in red. The inset figure shows the different recruitment profiles of Atg3-YPF depending on the PC/PE ratio.
E. The characteristic half concentration $C_{1/2}$ of ATG3-YFP binding from experiments done as described in C, D for the indicated PC/PE ratio.
F. Western blot of untagged ATG3 recombinant protein bound to liposomes and artificial lipid droplets in the top fraction of flotation assays.
G. Schematic representation illustrates droplet embedded vesicle (DEV) system.
H. Confocal imaging of a droplet embedded vesicle (DEV) made of 7/3 PC/PE and incubated with ATG3-YFP.

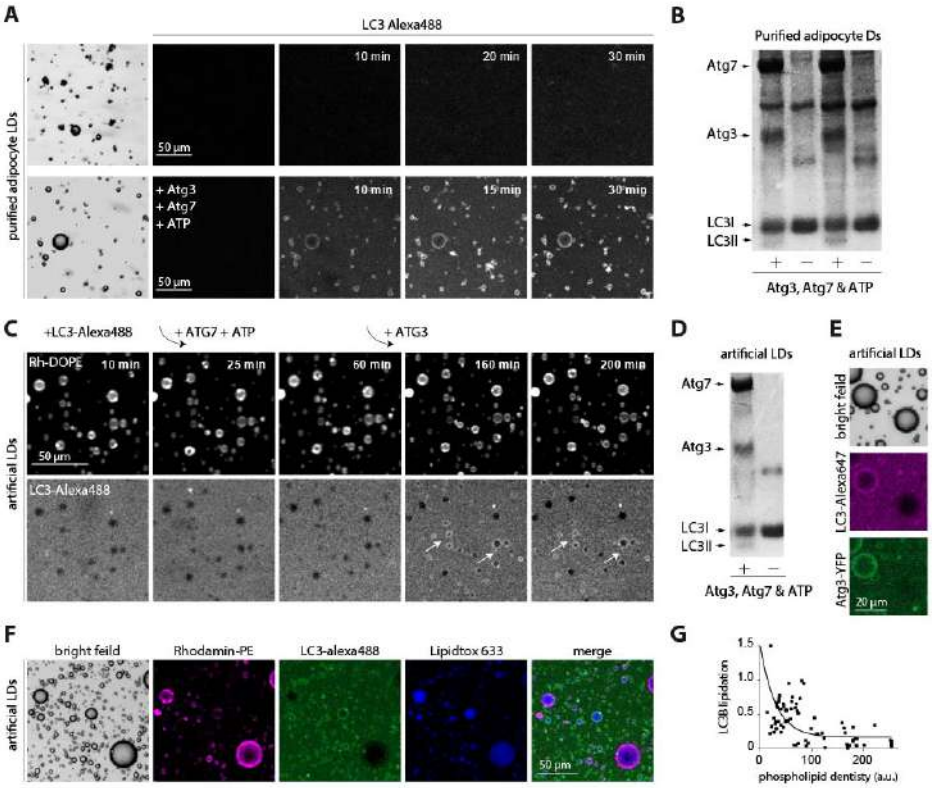

Figure 5

1017

Figure 5. Atg3 lipidates LC3 to LDs

A. To purified adipocyte LDs in HKM buffer are added or not the lipidation components, ATG7, ATG3, ATP, in presence of LC3B Alexa488.
B. LDs in the experiment in A are recovered and run in a Coomassie blue stained SDS–PAGE gel.
C. Confocal imaging of triolein-in-buffer droplets decorated by PC/PE (7/3) incubated with LC3B alexa488, then ATG7 and ATP. No lipidation occurred. Finally ATG3 was added. Lipidation occurred.
D. The artificial LDs in the experiment in C are recovered and run in a Coomassie blue stained SDS–PAGE gel.
E. Confocal imaging of triolein-in-buffer droplets decorated by PC/PE (7/3) at different monolayer phospholipid densities, based on Rho-PE signal. The droplets are incubated with LC3B-Alexa647 and Atg3/Atg3-YFP (80/20), ATP and ATG7.
F. Confocal imaging of triolein-in-buffer droplets decorated by PC/PE (7/3) at different monolayer phospholipid densities varied from 0.005% to 0.2% (w/w to triolein). They are incubated with LC3B-Alexa488 and Atg3 (80/20), ATP and ATG7.
G. Quantification of F. LC3B-Alexa488 lipidation to triolein droplets as a function of the phospholipid density.

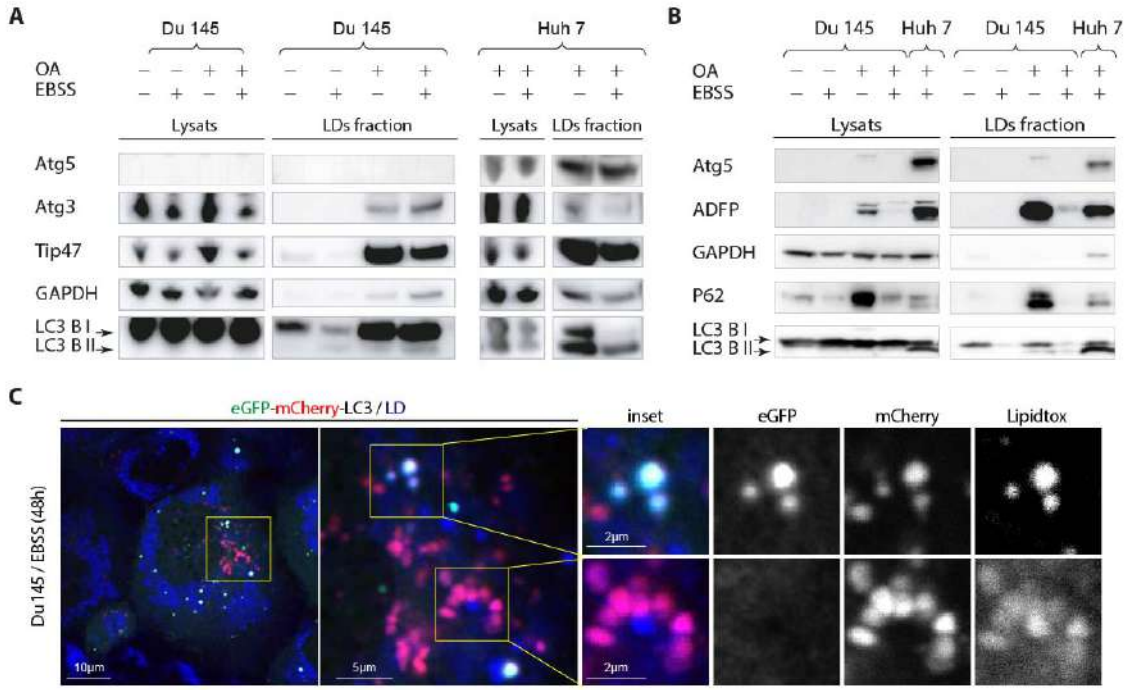

Figure 6

1094

Figure 6. LC3B-II is detectable on LDs of DU145 cells treated with OA

A. Western blot of Lysate and LD fractions from DU45 and Huh7 cells. Cells are grown in DMEM and treated or not with OA for 24hs, then incubated in DMEM or EBSS for 48h.
B. Western blot of Lysate and LD fractions of DU45 and Huh7 cells. Cells were grown in DMEM and treated or not with OA for 24hs then incubated in DMEM or EBSS for 48h.
C. Confocal imaging of LDs in eGFP-mcherry-LC3B stably-transfected DU45 cells. Cells are treated with oleic acid for 24h and then incubated in EBSS for 48h. Scale bar, 10 μm (5μm or 2μm in insets).

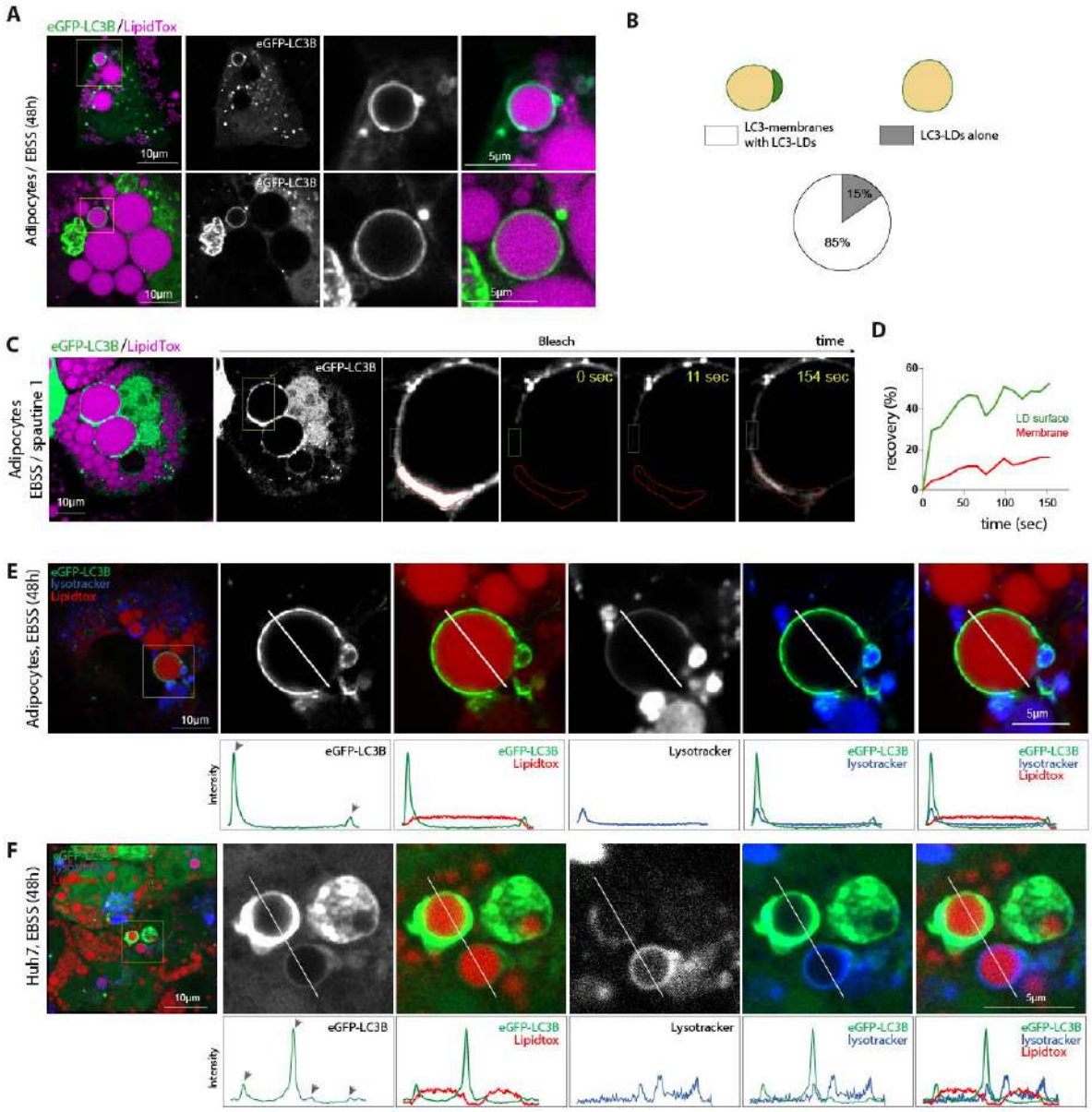

Figure 7

1136

Figure 7. LC3B-positive LDs interact with acidified autophagosome-like membranes

A. Confocal imaging of differentiated 3T3 L1 adipocytes virally transfected with eGFP-LC3B and LDs. Cells are incubated in EBSS for 48hs after transfection. Scale bar, 10 μm.

B. Schematic representation illustrating eGFP-LC3B-positive LDs with or without puncta. The sector graph shows the percentage of eGFP-LC3B-positive LDs with and without puncta. Quantifications are from three independent experiments.

C. FRAP analysis of eGFP-LC3B in differentiated 3T3 L1 adipocytes virally transfected with eGFP-LC3B and incubated in EBSS containing spautin 1 for 48hs. The insets indicate the bleached region: red for the autophagosome area and green for the LD surface. Scale bar, 10 μm.

D. Line graph shows the quantitative analysis of the recovery kinetics of eGFP-LC3B in the different regions depicted in C.

E. Confocal imaging of eGFP-LC3B, (lysotracker blue) and LDs in differentiated 3T3 L1 adipocytes virally transfected with eGFP-LC3B. Cells are incubated in EBSS for 48hs after transfection. Scale bar,10 μm (5 μm in insets). Bottom panels are line graphs showing the intensity line profile of the line drawn on in each image.

F. Confocal imaging of eGFP-LC3B, (lysotracker blue) and LDs in Huh7 loaded with oleic acid for 24hs and virally transfected with eGFP-LC3B. Cells are then incubated in EBSS for 48hs after transfection. Scale bar,10 μm (5 μm in insets). Bottom panels are line graphs showing the intensity line profile of the line drawn on in each image.

EXPERIMENTAL PROCEDURE

Plasmids

pATG3 dsRED was prepared by cloning ATG3 into the dsRED-N1 vector via EcoR1/Kpn1 restriction sites. FUGW ATG3 dsRED Expressing C-terminal tagged DsRED: ATG3 dsRED gene were amplified from pATG3dsRED and cloned in FUGW plasmid. FUGW ATG3 EGFP expressing N-terminal tagged ATG3: ATG3 gene were cloned into FUGW.
PLIN1 mCherry was a gift from D. Savage group. ATGL was gift from Carole Sztalryd.
pMRXIP SECFP-Stx17TM was a gift from Noboru Mizushima (Addgene plasmid # 86777; http://n2t.net/addgene:86777; RRID: Addgene_86777). pBABE-puro mCherry-EGFP-LC3B was a gift from Jayanta Debnath (Addgene plasmid # 22418; http://n2t.net/addgene:22418; RRID: Addgene_22418). psPAX2 was a gift from Didier Trono (Addgene plasmid # 12260; http://n2t.net/addgene:12260; RRID: Addgene_12260). pCMV-VSV-G was a gift from Bob Weinberg (Addgene plasmid # 8454; http://n2t.net/addgene:8454; RRID: Addgene_8454)
pUMVC was a gift from Bob Weinberg (Addgene plasmid # 8449;
http://n2t.net/addgene:8449; RRID: Addgene_8449)

Antibodies

Primary antibodies:

Anti LC3B Rabbit polyclonal anti body (abcam #ab48394), Anti-GABARAP + GABARAPL1 + GABARAPL2 Rabbit monoclonal antibody (abcam # ab109364), Anti ATG3 Rabbit monoclonal antibody (abcam # ab108251), Anti ATG3 Mouse monoclonal antibody (santa crus# c-393660), Anti-ADFP Rabbit polyclonal antibody (abcam # ab52355), anti PLIN3 Rabbit polyclonal antibody (Sigma Aldrich # HPA006427), Anti-SQSTM1 / p62 Mouse monoclonal antibody (abcam# ab56416), anti B-actin mouse monoclonal HPR conjugated anti body (Santa Cruz biotech # Sc-47778), anti GAPDH mouse monoclonal HPR conjugated anti body (ThermoFisher # MA5-15738-HPR).

Secondary antibodies:

anti-rabbit HPR conjugated (ThermoFisher # SA1-200), anti-mouse HPR conjugated (ThermoFisher # A16011), Anti Goat HPR conjugated (A15999 invetrogen), Donkey anti Goat DyLight 650 (ThermoFisher # SA5-10089), Donkey anti-Rabbit Alexa Fluor 568 (Invitrogen # A10042), Donkey anti-Rabbit Alexa Fluor 488 (Invitrogen # A21206), Donkey anti-Mouse Alexa Fluor 568 (Invitrogen # A10037).

Cell lines and culture conditions

Human hepatocarcinoma cells Huh7, HeLa cells, Adipocytes 3T3 L1, DU45 cells were used in this study. HeLa, Huh7, DU45 cells were maintained in High Glucose with stabilised Glutamine and with Sodium Pyruvate Dulbecco's modified Eagle's Medium (DMEM) (Dutscher) supplemented with 10% heat-inactivated fetal bovine serum and 1% penicillin/streptomycin (GibcoBRL). This medium is named further as DMEM.
Preadipocytes 3T3 L1 were maintained in Dulbecco's modified DMEM High Glucose with stabilised Glutamine, with Sodium Pyruvate supplemented with 10% new born calf serum Gibco and 1% penicillin/streptomycin (GibcoBRL).

Stably transfected cell lines generation:

Huh7 cells were transfected with shRNA Atg3 (h) Plasmide (Santa Cruz biotech # Sc-72582-SH) for 48h then untransfected cells were removed by Puromycin dihydrochloride (Santa Cruz biotech # Sc-108071) selection.
DU145 LC3B eGFP mCherry stably transfected cells:
HEK T293 cells were transiently transfected with retroviral vectors ((pCMV-VSV-G Addgene plasmid # 8454, pUMVC Addgene plasmid # 8449, pBABE-puro mCherry-EGFP-LC3B Addgene plasmid # 22418) using lipofectamine 2000 reagent. After culture for 72 hr, the growth medium containing retrovirus was collected. DU145 cells were incubated with the collected

virus-containing medium for 24 hr. Uninfected cells were removed by Puromycin dihydrochloride (Santa Cruz biotech # Sc-108071) selection.

Adipocytes differentiation

Confluent preadipocytes 3T3 L1 cells were incubated in a differentiation medium composed of the growth medium containing 0.25 µM dexamethazone, 10 µg/ml insulin, and 0.5 mM 3-isobutyl-1-methylxanthine for 48h. The cell culture medium was changed to post differentiation medium composed of growth medium containing 5 µg/ml insulin and incubated in this medium for 48h then in fresh growth media for 24h. The differentiated adipocytes were used for subsequent experiments.

Modulation of Autophagy

To inhibit autophagy in nutrient starvation condition, 3-Methyladenine (3-MA) (Sigma Aldrich # SAE0107) was used at final concentration of 5 µM. Chloroquine (Sigma Aldrich Cat: C6628) and Spautin-1 (Sigma Aldrich Cat: SML0440) at final concentration of 100 µM and 10 µM respectively. Autophagy was induced using rapamycin at final concentration of 500nM.

Oleic acid treatment

When indicated, cells (60–70% confluence) were incubated for 24h with the growth medium supplemented with 200 µM oleic acid conjugated to bovine serum albumin (BSA) (1% vol/vol) to induce LDs formation and accumulation.

Cells transfection

Cells were transfected with indicated plasmid using Polyethyleneimine HCl MAX (Polysciences) following the manufacturer's instructions.

Virus mediated gene transductions

Viral particles:

eGFP-LC3B adenovirus was kindly provided by Sharon Tooze (London Research Institute, UK) and was amplified in QBI-HEK 293A cells and purified on a cesium chloride gradient.
ATG3 shRNA (MISSION® shRNA Lentiviral Transduction Particles cat: SHCLNV-NM_022488 Sigma Aldrich). ATG5 shRNA (MISSION® shRNA Lentiviral Transduction Particles cat: SHCLNV-NM_004849 Sigma Aldrich). P62 RFP BacMam reagents (insect Baculovirus with a Mammalian promoter) (Premo Autophagy Sensor p62 kit, Molecular Probes cat: P36241)

Virus-mediated gene transductions were performed as following: HeLa, Huh7 and DU45 at 60-70% of confluence or differentiated Adipocytes were incubated with the culture medium containing the viral particles at MOI=10. After incubation at 37 °C for 16 h, the inoculum was removed then cells were washed three times with fresh medium and were further maintained in indicated culture medium.
Transduction of p62: Differentiated adipocytes were transduced with (Premo Autophagy Sensor p62 kit, Molecular Probes cat: P36241) at MOI=10. After 18 h, the cells were washed twice with DPBs then subjected to feeding and nutrient starvation condition for indicated time.

Lipid Droplets purification:

Cells were washed twice with ice-cold PBS. Then, cells were scraped into a homogenization buffer comprising 10 mM Tris/HCl, 1 mM EGTA, 0.5 mM EDTA, at pH 7.4, and contained Complete™ protease inhibitors. Cells were inculpated in ice for 15 minutes. The result solution loaded into a syringe and passed rapidly ten times within 18G needle to mechanically disrupt the cells. Post-nuclear supernatants (PNS) were obtained by centrifugation for 10 min at 1000 g. PNS was mixed with Iodixanol solution (OptiPrep cat: D1556 Sigma Aldich) at 35% (w/w). 1ml of this solution was loaded to the bottom of 3 ml centrifugation tub and two successive layers of 850 µl of 20% (w/w) and 10 % (w/w) of Iodixanol in the homogenization buffer were

added. Then one layer of 200µl of homogenization buffer was added. The gradients were centrifuged for at least 16 h at 175,000 rpm. LDs were harvested from the top of the gradients.

Immunoblot

Cells were washed twice with ice-cold DPBS and lysed on ice using the RIPA LYSIS BUFFER (Thermo Fisher cat:89900) containing protease inhibitors (complete ULTRA Cat: 05892970001 Roche). High lipid containing samples such as the lysate of cells treated with oleic acid, differentiated adipocytes and purified LDs were delipidated to get rid of the high quantity of lipids which affects the separation of protein by SDS PAGE. Briefly, 1 volume of TCA (100%W/V) was add to 4 volumes of protein sample then incubated on ice for 10 minutes. Samples were centrifuged at 14000 RPM for 10 minutes and the supernatant was discarded. Pellet was washed twice with 200µl cold acetone then drayed. the drayed pellet was resuspended in RIPA LYSIS BUFFER containing 1X NuPAGE LDS Sample Buffer (Thermo Fisher Cat: NP0007) then heated at 95°C for 7 minutes. The proteins were separated on SDS–PAGE and electro-transferred onto nitrocellulose membrane. After transfer, the membrane was saturated in DPBS containing 0.1% Tween 20 and 5% milk. Primary antibodies were added overnight at 4 °C or for 2 h at room temperature depending on the antibody. The membranes were washed with DPBS containing 0.1% Tween and incubated for 1 h at room temperature with appropriate HRP conjugated secondary antibody. ECL plus kit (Thermo Scientific Cat: 32132) or Substrat chemiluminescent SuperSignal™ West Femto (Thermo Sceintific Cat: 34095) was used for protein detection. Blot quantification was done using ImageJ software.

Immunofluorescence staining:

Cells were grown on coverslips, fixed with 4% paraformaldehyde for 20 min. and permeabilized for 20 min. at 37°C using a permeabilizing buffer (PFS): DPBS containing saponin (Cat: 10294440 Fisher Scientific) 0.025% m.v−1 and gelatin from cold water fish skin (Cat: G7041 Sigma 0.7% m.v−1). The cells were then incubated with primary antibody for 2 h and washed three times for 5 min with PFS before being incubated with the appropriate secondary antibodies or with the dye for 90 min. The coverslips were mounted using Prolong Gold (Cat: P36934, Invitrogen).

Image acquisition and analysis

Images acquired with a Leica TCS SP5 AOBS tandem confocal microscope and ZEISS LSM 9 with Airyscan. For live imaging cells were grown in MatTek 3.5mm coverslip bottom dishes. For colocalization analysis, images were treated with ImageJ software, and the 'Intensity Correlation Analysis' plug-in was used to generate Pearson's correlation coefficient (Rr) values which ranged from −1 (perfect exclusion) to +1 (perfect correlation).

Protein expression & purification for human Atg8 homologs and ATG3.

Human LC3B and GABARAPL1 (mammalian Atg8 homologs) were cloned into PGEX-2T GST and mouse ATG3 was cloned into PGEX-6p and then expressed and purified essentially as described in Motta et al bioRxiv 348730. In brief: To facilitate *in vitro* lipidation, each is expressed with a COOH-terminal truncation such that the protein sequence ends with the reactive glycine (G120 in LC3B and G116 in GABARAPL1). To facilitate dye-labeling, LC3B and GABARAPL1 were mutated with Quik Change II Site-Directed Mutagenesis Kit (Agilent Technologies) to include a cysteine immediately before the start methionine of the natural protein sequence. In this organization, there remain two additional amino acids N-terminal to the cysteine which derive from the thrombin cleavage site used to release GST.

LC3B, GABARAPL1 and ATG3 proteins were expressed in BL21-Gold (DE3) Competent Cells (Agilent Technologies). Cells were cultured in 2L Luria Bertani Broth (LB) media with 1:1000 carbenicillin (50 mg/mL) and induced with IPTG (0.5 mM final). Cells were collected by centrifugation and treated with EDTA-free protease inhibitor cocktail tablets in either thrombin buffer (20 mM Tris pH 7.5, 100 mM NaCl, 5 mM MgCl2, 2 mM CaCl2. 0.2 mM TCEP) for

LC3B/GABARAPL1 or precision protease buffer (50 mM Tris pH 7.5, 150 mM NaCl, 1 mM EDTA, 1 mM DTT) for ATG3. Cells were lysed via three passages through a cell disrupter. To purify, lysate was incubated with glutathione beads for 3 hours at 4°C. Beads were washed several times and then incubated with LC3B/GABARAP cutting buffer (10 uL thrombin + 500 uL thrombin buffer + 0.2 mM TCEP + 500 uL beads) or ATG3 cutting buffer (25 uL precision protease + 500 uL precision protease buffer + 1 mM DTT + 500 uL beads) overnight. Purified proteins were stored in 20% glycerol at -80°C.

Protein expression & purification for human ATG7.

Human ATG7 in pFastBac vector was from Sloan-Kettering (kind gift of X. Jiang) and was expressed in baculovirus and purified via nickel beads as previously described (Nath et al., 2014). The plasmid was transformed into Bacmid DNA. SF9 cells were transfected via Cellfectin II and grown for 72 hours. Cells were treated with EDTA-free protease inhibitor cocktail tablets in lysis buffer (20 mM Tris pH 8, 500 mM NaCl, 20 mM Imidazole, 1 mM DTT, 10% glycerol), sonicated with a Virsonic 600 (VirTis) microtip for 3 minutes in a 30 sec on, 30 sec off cycle at speed 3.5, then centrifuged at 18000 rpm for 1 hour. Lysate was then incubated with 1 mL Nickel resin (Ni-NTA Agarose) for 2 hours at 4°C, before washing beads with 20 mM Tris pH 8, 300 mM NaCl, 20 mM Imidazole, 1 mM DTT three times. To elute beads were washed with 20 mM Tris pH 7.5, 300 mM NaCl, 500 mM Imidazole, 1 mM DTT. Purified proteins were stored in 20% glycerol at -80°C.

In vitro experiments.

Purified lipid droplets were obtained as described above. In vitro experiments were performed in HKM buffer: 50 mM HEPES, 120 mM potassium acetate, and 1 mM MgCl2 (in Milli-Q water) at pH 7.4. For LC3 lipidation experiments on purified lipid droplets, 10 µL of the recovered cellular LDs fractions was mixed with 200 µl of HKM and then injected in the observation chamber. The protein machinery was next added to the mixture and imaging was done for one to two hours at 37°C.

Lipids and preparation of the Oil Phase.

Phospholipids (phosphatidylcholine (PC) and phosphatidylethanolamine (PE)) used for giant unilamellar vesicles and artificial Lipid droplets formation were purchased from Avanti Polar Lipids, Inc. Chloroform which was dissolving the lipids was evaporated under a stream of argon; the dried lipids were subsequently re-solubilized to the desired concentration in the oil phase triolein (TO) which was purchased from NuChek Prep (Elysian, MN). It was > 99% pure and its interfacial tension at 25.0°C was 32 ± 1 mN/m. Lipid concentrations ranging from 0.1 to 2 % w/w were tested for Atg3 binding experiments, all of which were above the critical concentration for forming stable artificial droplet, i.e. no fusion between droplets. Rhodamin-PE 1% w/w (final solution) was used to visualize the monolayers and bilayers interfaces.
Unless mentioned, in vitro experiments were performed in the following HKM buffer: 50 mM Hepes, 120 mM Kacetate, and 1 mM MgCl2 (in Milli-Q water) at pH 7.4.

Giant Unilamellar Vesicles and Artificial Lipid Droplets Formation.

GUVs were prepared by electroformation. Mixture of DOPC and DOPE 70:30 in chloroform at 0.5 mM was dried on an indium tin oxide (ITO)-coated glass plate. The lipid film was desiccated for 1 h. The chamber was sealed with another ITO- coated glass plate. The lipids were then rehydrated with a sucrose solution (275 mOsm). Electroformation is done using 100 Hz AC voltage at 1.0 to 1.4 Vpp and maintained for at least 1 h. This low voltage was used to avoid hydrolysis of water and dissolution of titanium ions glass plate. GUVs were either stored in the chamber at 4°C overnight or directly collected with a Pasteur pipette.

To prepare the artificial lipid droplets aLDs, 5 µL of the lipid oil solution was added to 45 µL of HKM buffer. The mixture was sonicated. The diameter of the resulting droplets is a few hundred nanometers. The aLDs were then injected in the observation chamber made with two-glass coverslips assembled with 100 mm thick double-sided tape, pre-treated with 3 % wt/v BSA and

washed three times with HKM buffer. Once the drops reached the top of the chamber, the protein mixture was added to the buffer and observed one to two hours at 37°C.

Interfacial tension measurements.

Interfacial tension measurements were performed using a drop tensiometer device designed by Teclis Instruments (Tracker, Teclis-IT Concept, France) to measure the interfacial tension of oil – water interfaces. In our experiments the pendant drop is the triolein lipid phase, formed in the aqueous HKM buffer. The triolein – water interface stabilizes at ~32.0 ± 1 mN/m. When indicated the lipid phase contains 0.005% of phospholipids and tension stabilized at 25 - 27 mN/m. Adsorption of Atg3 translated into an decrease in tension, as it masked the oil-water interface. Throughout the adsorption kinetics to either a triolein – water or a phospholipid-covered triolein – water interface, the drop area was maintained constant.

At the equilibrium tension, we submitted to the drop series of compressions and re-expansions (by withdrawing the droplet volume at a speed of - 0,01 mm^3/s). The sudden decrease in volume induced a decrease in drop surface area, resulting in a sudden compression and abrupt decrease in tension. The oil drop was held at this reduced volume for 5–10 min, with tension being recorded. Each surface tension experiment was determined by this mean three measurements were performed for each lipid condition studied. All experiments were conducted at 25.0 ± 0.2°C in a thermostated system.

FRAP experiments.

For FRAP experiments, we bleached the signal on a collection of drops and monitored the increase of signal during recovery. The background signal, for example, from the cytosol, was removed from the recorded signal, which was at the end normalized by intrinsic bleaching of nonbleached areas. We next used GraphPad Prism to fit the FRAP recovery curves with a nonlinear regression and the exponential one-phase association model.

Protein Labelling.

Alexa Fluor488 or C5-maleimide (Alexa488) and Alexa Fluor647 or C5-maleimide were purchased from Life Technologies. LC3-N-Cys and GABARAPL1-N-Cys were labelled with Alexa Fluor488/647 C5-maleimide through the amino-terminal cysteine. LC3-N-Cys protein (100 µM) was mixed with 600 µM TCEP. After 5 min of incubation at room temperature, the fluorescent dye (800 µM) dissolved in DMSO was added. The mixture was protected from light and slowly mixed at room temperature for 2 h or overnight at 4 °C. The labelled LC3 was then dialyzed to get rid of free dye in order to reduce the background fluorescence in Tris-NaCl buffer (50 mM trizma hydrochloride, 100 mM NaCl, at pH 7.6) overnight at 4 °C on stirrer.

Quantification and statistical analysis

Unpaired Student's t-tests or ordinary one-way ANOVA test (*** P<0.0001) were performed and statistical significance was determined at *P <0.05, ** P <0.001 and ***P < 0.0001.
All values shown in the text and figures are mean ± SEM, from indicated n independent experiments.